SEARCH FOR HIGH-MASS RESONANCES DECAYING INTO LEPTONS OF DIFFERENT FLAVOR (eμ, eτ, $\mu\tau$) IN $P\bar{P}$ COLLISIONS AT $\sqrt{S} = 1.96$ TeV

Yanjun Tu

A DISSERTATION

in

Physics and Astronomy

Presented to the Faculties of the University of Pennsylvania in Partial Fulfillment of the Requirements for the Degree of Doctor of Philosophy

2008

Nigel S. Lockyer
Supervisor of Dissertation

Ravi K. Sheth
Graduate Group Chairperson

Acknowledgements

I would like to take this opportunity to acknowledge all who had helped me during my Ph.D. study in Physics and Astronomy Department at University of Pennsylvania.

First and foremost, I must acknowledge Professor Nigel S. Locker, my thesis advisor, and Dr. Pavel Murat, my mentor at Fermilab, for their enthusiastic help during my Ph.D. study. Professor Nigel S. Locker led me into the beautiful word of experimental particle physics, and Dr. Pavel Murat broadened my insight in this research. I am so fortunate to have had the opportunity to study and work under their stimulating and encouraging advise. I will go further in my academic life benefiting from their advice.

I also want to acknowledge Dr. Anadi Canepa, closely working together with me, in addition to the physics, I also learned from her how to schedule my work in a more efficient way and never give up. I would like to give my thanks to Dr. Joel Heinrich for his wise and patient explanations on all kinds of physics and statistical questions.

It is my pleasure to extend gratitude to Professor Mirjam Cvetič, Professor Joe Kroll, Professor Paul Langacker, Professor Evelyn Thomson and Professor Brig Williams. My thesis was finished under their wonderful help. I would also like to say thanks to Walter Kononenko and Jean O'Boyle for their nice support.

I am grateful to my colleagues as well, both postdoctorals and students, for their friendship and useful discussions on physics. I would like to thank specially Dr. Chris Neu, Dr. Kristian Hahn, Dr. Aart Heijboer, Dr. Peter Wittich, Dr. Shi-Shan

Yu, Dr. Daniel Whiteson, Justin Keung, Elisabetta Pianori and Tatiana Rodriguez.

Finally, I would like to acknowledge my parents and my husband. Without their full and strong support throughout these years, it would be impossible for me to achieve this, and so much else.

ABSTRACT

SEARCH FOR HIGH-MASS RESONANCES DECAYING INTO LEPTONS OF DIFFERENT FLAVOR (eμ, eτ, $\mu\tau$) IN $P\bar{P}$ COLLISIONS AT $\sqrt{S} = 1.96$ TeV

Yanjun Tu

Nigel S. Lockyer

We present a search for high-mass resonances decaying into two leptons of different flavor: $e\mu$, $e\tau$ and $\mu\tau$. These resonances are predicted by several models beyond the standard model, such as the R-parity-violating MSSM. The search is based on 1 fb^{-1} of data collected at the Collider Detector at Fermilab (CDF II) in proton anti-proton collisions. Our observations are consistent with the standard model expectations. The results are interpreted to set 95 % C.L. upper limits on $\sigma \times$ BR of $\widetilde{\nu}_\tau \rightarrow e\mu, e\tau, \mu\tau$.

Contents

List of Figures

List of Tables

Chapter 1

Introduction

At the start of the twentieth century, since the discovery of the electron by Joseph Thompson in 1898, scientists started to probe the microscopic world and asked what are the most basic constituents of matter and how do they interact. By the middle of the twentieth century, the known leptons were the electron, the muon and their two neutrinos; hadrons, such as protons and pions, and quantum mechanics were accepted as the fundamental precepts of physics. In the middle of 1960's, C. N. Yang and R. Mills published a paper on the isotopic $SU(2)$ invariance of the proton-neutron system, the basic principles of which has become known as Yang-Mills theory. The theory is now a cornerstone of the standard model of particle physics. Meanwhile, physicists realized that their previous understanding, where all matter is composed of the fundamental protons, neutrons, and electron, was insufficient to explain the new particles being discovered. Therefore, M. G. Mann and G. Zweig proposed the quark model in 1964. The picture of the standard model became gradually clear when its two compositions were formed: the electroweak theory, unifying the electromagnetic and weak force, created by S. Weinberg, S. Glashow and A. Salam in 1967, and the quantum chromodynamics field theory of strong interactions formulated in 1973. The discovery of the charm quark in 1974 through the J/ψ meson confirmed the success of QCD. The $W^{\pm}$ and Z^0 gauge bosons, carriers of electroweak forces predicted by

QED, were observed at CERN in 1983. The standard model was confirmed. In 1995, the discovery of the top quark by the CDF and D0 experiments at Fermilab convinced physicists the correctness of the standard model.

Nevertheless, the discovery of dark matter and dark energy, the evidence of neutrinos having mass, together with other puzzles, suggested that the standard model is not the ultimate theory. To address many questions not answered in the standard model, we need new physics. Besides the particles which have been observed, there are many particles predicted by new physics yet to be discovered. These undiscovered particles, expected to be heavier than most standard model particles, can be created and detected during energetic collisions between particles in accelerators. As the current highest energy particle accelerator, the Tevatron at Fermi National Laboratory provides promising chances of new particle discoveries.

In this thesis, we report a search for high-mass resonances decaying into two leptons of different flavor: $e\mu$, $e\tau$ and $\mu\tau$. The search is based on 1 fb^{-1} of data collected at the Collider Detector at Fermilab (CDF II) in proton anti-proton collisions. These processes, violating both lepton number and lepton flavor number, are not allowed in the SM, but are expected in many new physics models, e.g., sneutrino decay in the supersymmetric model with R-parity violation, Z' gauge boson decay in the non-universal $U(1)'$-model and Higgs decay in the two Higgs doublet model. Any discovery therefore will be a proof of the new physics. The search is interesting because it is the first probe to R-parity violating couplings related to the third generation lepton tau in a direct search. Technically, this search is very challenging because we can only use the hadronic decay mode of the tau in order to distinguish taus from the prompt electron and muon in the final states, where the hadronic taus have a less accurate energy measurement, lower identification efficiency, and higher background compared to the other charged leptons. In order to increase the signal acceptance and reduce the background in tau channels, we have made several improvements, which will be discussed in the thesis. In Chapter I and II, we introduce

the physics motivation and the CDF detector. In Chapter III, we describe the lepton identification. In particularly, we focus on the tau lepton identification, which is the most challenging part of this analysis. In Chapter IV and V, we describe how the search was performed and the results.

Chapter 2

Physics

2.1 The Baryon Number and Lepton Number Symmetries in the Standard Model

The Standard Model (SM) is a $SU(3)_C \times SU(2)_L \times U(1)_Y$ gauge theory[1] used to describe microscopic interactions. According to the SM, before electroweak symmetry breaking, the fundamental fermions interact via either the strong interaction (described by $SU(3)_C$) or electroweak interaction (described by $SU(2)_L \times U(1)_Y$), which are mediated by twelve massless gauge bosons related to the gauge symmetries. With the electroweak symmetry $SU(2)_L \times U(1)_Y$ broken down to $U(1)_{EM}$, three of the twelve SM gauge bosons, *i.e.*, $W^{\pm}$ and Z^0, obtain mass and become the mediators of the weak interactions, where $W^{\pm}$ are gauge bosons of $SU(2)_L$ and Z^0 is a mixing of the third gauge boson of $SU(2)_L$ and the $U(1)_Y$ gauge boson. The remaining massless gluons and γ mediate the strong and electromagnetic interactions. In the SM, the fundamental fermions are grouped into 3 families. Each family contains 15 fundamental fermions which are listed in Table 2.1. These fundamental

[1]Gauge theory means that the Lagrangian of the system is invariant under the related gauge transformation, where "gauge" implies that the infinitesimal transformation parameters are space-time dependent.

names	spin 1/2	$SU(3)_C$, $SU(2)_L$, $U(1)_Y$
quarks	$(u_L\ d_L)$	$(\mathbf{3}, \mathbf{2}, \frac{1}{6})$
	$\overline{u}_R$	$(\overline{\mathbf{3}}, \mathbf{1}, -\frac{2}{3})$
	$\overline{d}_R$	$(\overline{\mathbf{3}}, \mathbf{1}, \frac{1}{3})$
leptons	$(\nu_L\ e_L)$	$(\mathbf{1}, \mathbf{2}, -\frac{1}{2})$
	$\overline{e}_R$	$(\mathbf{1}, \mathbf{1}, 1)$
gluon	g	$(\mathbf{8}, \mathbf{1}, 0)$
hypercharge gauge boson	B^0	$(\mathbf{1}, \mathbf{1}, 0)$
isospin gauge boson	$W^{\pm}, W^0$	$(\mathbf{1}, \mathbf{3}, 0)$
Higgs boson	H	$(\mathbf{1}, \mathbf{2}, \frac{1}{2})$

Table 2.1: **Field Contents in the SM.**

fermions carry quantum "charges", which correspond to the gauge group generators, reflecting how they interact via the related forces. For example, the quarks can interact via the strong force because they carry the $SU(3)_C$ charge "color". The fundamental particles can interact via electroweak interactions if they carry "weak isospin" or "hypercharge", which correspond to $SU(2)_L$ and $U(1)_Y$, respectively. As for the electric charge familiar to us, it is a relic of electroweak symmetry breaking, related to the weak isospin and the hypercharge according to $Q = T_3 + Y$. Here T_3 is the third component of the weak isospin and Y is the hypercharge. In addition to the gauge bosons and the fundamental fermions, a hypothesized scalar particle, the Higgs, is predicted to give the fundamental particles mass during the electroweak symmetry breaking (Higgs mechanism).

The SM has been very successful in several aspects:

1. it explains the three fundamental interactions of elementary particles that make up all matter, the strong, weak and electromagnetic interactions with the same mathematical form—Yang-Mills gauge theories.

2. it unifies the weak and the electromagnetic forces.

3. it predicts the existence of W and Z bosons, the gluon, the top quark and the charm quark before these particles had been observed.

4. some aspects of the SM have been tested precisely, e.g. the electroweak mixing angle.

Besides the gauge symmetries, there are some global symmetries like Baryon number (B) symmetry and Lepton number (L) symmetry, which means that B and L remain unchanged after interactions[2]. The conservation of B and L is an "accidental" symmetry arising from the nature of the operators in the theory— there are no renormalizable[3] Lagrangian terms which violate B or L. In reality, all the observed interactions conserve B and L, for instance, the beta decay: $n \to p + e^- + \overline{\nu}_e$, conserves B and L. In particular, if the proton would decay, the processes (e.g. $p \to e^+ + \pi^0$ or $p \to u^+ + K^0$) must violate B and L since the proton is already the lightest baryon. In fact, the proton decay has not been observed. However, the B and L symmetries are not anomaly free, which means that in loop level interactions, B and L are not conserved. Therefore they are not exact symmetries, although $B-L$ is an exact symmetry because the anomaly of B is canceled by the anomaly of L.

2.2 R-Parity Violating Minimal Supersymmetric Standard Model

The SM is not the ultimate theory. The quantum corrections to the square of the Higgs mass are quadratically divergent (the hierarchy problem). The SM Higgs boson has not been observed. In addition, the SM fails to:

1. unify the strong and electroweak forces.
2. explain the neutrino masses and mixing.
3. include the force of gravity.
4. explain dark matter and dark energy
5. explain the asymmetry of matter and antimatter in the universe.

[2]In the SM, the leptons carry the lepton number $L = +1$ and anti-leptons carry $L = -1$, while the quarks are assigned the baryon number $B = +1/3$ and the anti-quark with $B = -1/3$.

[3]The SM is a renormalizable field theory containing only operators with mass dimension ≤ 4.

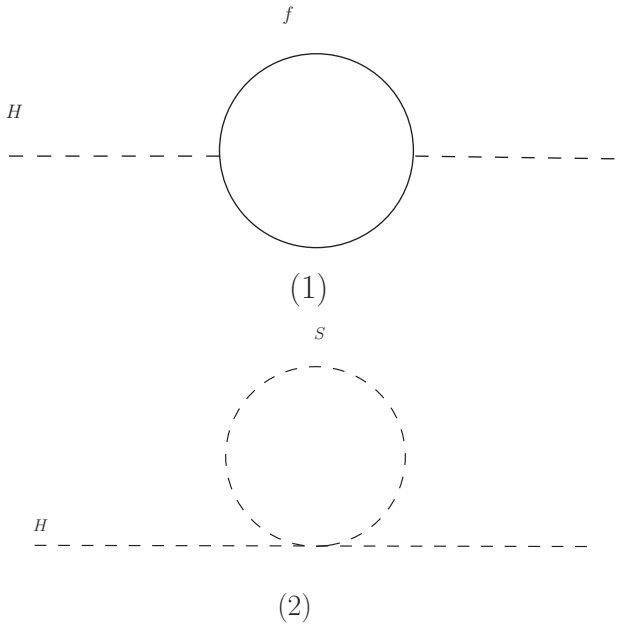

Figure 2.1: **One-loop Quantum Corrections to the Higgs Mass Squared.** (1) the corrections from a Dirac fermion f, (2) the corrections from a scalar S.

To address many open questions, we need new physics. Supersymmetry (SUSY) is one of the most promising theories beyond the SM. SUSY predicts that each SM particle has a supersymmetric partner with the same quantum numbers but the spin differing by 1/2. It provides a solution to the hierarchy problem because the quantum corrections to the Higgs mass squared are not quadratically divergent any more as the contribution from the SM particle is canceled out by the contribution from its superpartner (Fig. 2.1).

It realizes the unification of the strong, weak and electromagnetic interactions (Fig. 2.2). It also has other attractive aspects like providing a dark matter candidate, the lightest supersymmetric particle (LSP).

To provide a compact description of supersymmetry representations, the SM particle and their corresponding super-partner are built into a superfield since they

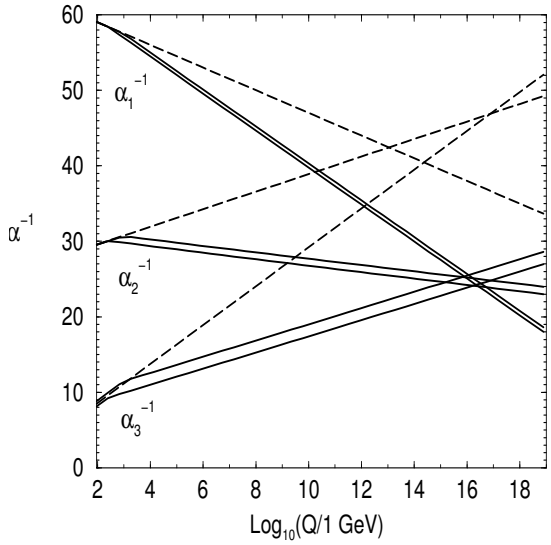

Figure 2.2: **Renormalization Group Evolution of the Gauge Couplings α_a^{-1}.** The unification of the gauge couplings is realized at a scale 10^{16} GeV in SUSY shown as the solid line.

transform in the same way under the gauge transformation. The superfield consisting of the fundamental chiral fermion is called the chiral superfield. The chiral superfields in the minimal supersymmetric standard model (MSSM), which is the minimal extension to the SM that realizes SUSY, are listed in the Table 2.2. Given a set of chiral superfields and a holomorphic function of them, which is defined as the superpotential W, a Lagrangian term which is invariant under supersymmetry can be constructed. The gauge invariant superpotential in MSSM is:

$$W_{\rm MSSM} \;=\; \bar{u}\, y_u\, Q\, H_u \;-\; \bar{d}\, y_d\, Q\, H_d \;-\; \bar{e}\, y_e\, L\, H_d \;+\; \mu\, H_u\, H_d \qquad (2.1)$$

In SUSY, the slepton and squark have the same B and L as their superpartners. Unlike the SM, where the conservation of B and L is an "accidental" symmetry, in the supersymmetic extension of SM, there are superpotential terms that are gauge-invariant but violate either B or L (Eq. 2.2), while all the couplings are renormalizable.

Names		spin 1/2	spin 0	$SU(3)_C$, $SU(2)_L$, $U(1)_Y$
quarks, squarks	Q	$(u_L \;\; d_L)$	$(\widetilde{u}_L \;\; \widetilde{d}_L)$	$(\,\mathbf{3},\,\mathbf{2}\,,\,\frac{1}{6})$
	$\overline{u}$	$u_R^\dagger$	$\widetilde{u}_R^*$	$(\,\overline{\mathbf{3}},\,\mathbf{1},\,-\frac{2}{3})$
	$\overline{d}$	$d_R^\dagger$	$\widetilde{d}_R^*$	$(\,\overline{\mathbf{3}},\,\mathbf{1},\,\frac{1}{3})$
leptons, sleptons	L	$(\nu \;\; e_L)$	$(\widetilde{\nu} \;\; \widetilde{e}_L)$	$(\,\mathbf{1},\,\mathbf{2}\,,\,-\frac{1}{2})$
	$\overline{e}$	$e_R^\dagger$	$\widetilde{e}_R^*$	$(\,\mathbf{1},\,\mathbf{1},\,1)$
Higgsino, Higgs	H_u	$(\widetilde{H_u^+} \;\; \widetilde{H_u^0})$	$(H_u^+ \;\; H_u^0)$	$(\,\mathbf{1},\,\mathbf{2}\,,\,+\frac{1}{2})$
	H_d	$(\widetilde{H_d^0} \;\; \widetilde{H_d^-})$	$(H_d^0 \;\; H_d^-)$	$(\,\mathbf{1},\,\mathbf{2}\,,\,-\frac{1}{2})$

Table 2.2: **Chiral Supermultiplets in the MSSM.**

$$\begin{aligned} W_{\Delta L=1} &= \frac{1}{2}\lambda^{ijk} L_i L_j \bar{e}_k + \lambda^{'ijk} L_i Q_j \bar{d}_k + \mu^{'i} L_i H_u, \\ W_{\Delta B=1} &= \frac{1}{2}\lambda^{''ijk} \bar{u}_i \bar{d}_j \bar{d}_k \end{aligned} \tag{2.2}$$

where L, Q and H are the $SU(2)$ doublet superfields of leptons, quarks and Higgs; e, u and d are the $SU(2)$ singlet superfields of leptons and quarks; λ, λ' and λ'' are Yukawa couplings; the indices i, j and k denote fermion generations.

However, with the introduction of the superpotential in Eq. 2.2, the proton could decay into a lepton and a meson (e.g. $p \to e^+ + \pi^0$ or $p \to u^+ + K^0$) mediated by the super particle (Fig.2.3). The corresponding operators are $L_1 Q_1 \bar{d}_k$ from the L violating term and $\bar{u}_1 \bar{d}_1 \bar{d}_k$ from the B violating term. The product of the couplings $\lambda'_{11k}\lambda''_{11k}$ is strongly constrained by the non-observation of proton decay.

To avoid proton decay, R-parity, defined as ($P_R = (-1)^{3(B-L)+2s}$, where s is the spin of the particle), is introduced. By definition, all the SM particles have R-parity of 1 while the supersymmetric particles have R-parity of -1. If R-parity is conserved, the interactions in Eq. 2.2 are forbidden. However, if the B and the L are not violated at the same time, the proton would not decay. Therefore R-parity violating (RPV) interactions conserving either the L or the B are viable.

Therefore it is well-motivated from both theoretical and experimental points of view to study R-Parity violating (RPV) interactions.

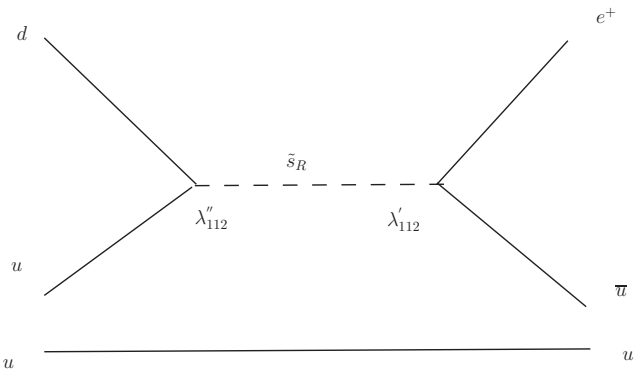

Figure 2.3: **Proton Decay.** The process $p \rightarrow e^+\pi^0$, mediated by the super partner of the right-handed s quark, violates both L and B.

There are 48 RPV couplings in Eq. 2.2. To satisfy the experimental bounds in the RPV framework, one generally introduces some alternative discrete symmetry which is weaker than R-parity, but enough for escaping experimental constraints. Experimentally, we take such a strategy: assume that one RPV coupling is dominant at a time while the others are negligible. In particular, some of these RPV couplings are not strongly constrained. Those less constrained couplings are studied in low energy experiments and high energy experiments. For example, the couplings λ_{13k} and λ_{23k} are constrained by the leptonic decay of taus: $\tau \rightarrow e\nu_\tau\nu_e$ and $\tau \rightarrow \mu\nu_\tau\nu_\mu$. The experimental value of the ratio R^{exp}, $BR^{exp}(\tau \rightarrow e\nu\overline{\nu})/BR^{exp}(\tau \rightarrow \mu\nu\overline{\nu}) = 1.0289 \pm 0.0075$, is consistent with the value predicted by the SM ($R^{SM} = 1.0282$) given the experimental uncertainty. However, if SUSY particles are involved in the process (Figure 2.4), the difference between the R^{exp} and R^{SM} can be translated to the limit of RPV couplings ($|\lambda_{13k}| < 0.05 \times (m(\tilde{e}^k_R)/100\ \mathrm{GeV/c^2})$ and $|\lambda_{23k}| < 0.05 \times (m(\tilde{e}^k_R)/100\ \mathrm{GeV/c^2})$ [4], where $m(\tilde{e}^k_R)$ is the mass of the kth generation right handed e-type slepton. The couplings λ'_{31k} are constrained by hadronic decay of $\tau \rightarrow \pi\nu_\tau$. If SUSY particles are involved in the process (Figure 2.5), the value of $BR^{exp}(\tau \rightarrow \pi\nu_\tau)/BR^{SM}(\tau \rightarrow \pi\nu_\tau)$ is translated to the limit of RPV coupling $|\lambda'_{31k}| < 0.10 \times (m(\tilde{d}^k_R)/100\ \mathrm{GeV/c^2})$ [4], where $m(\tilde{d}^k_R)$ is the mass of the kth generation right

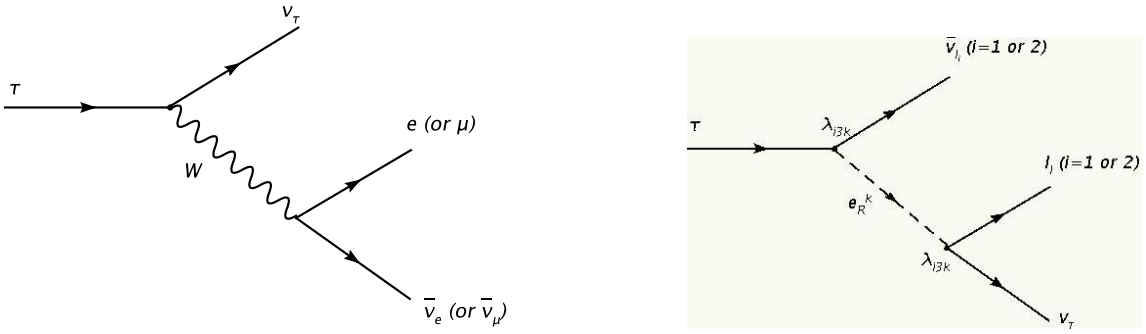

Figure 2.4: **Processes Contributing to the Measurement of λ_{i3k}.** The limits on λ_{i3k} come from measurements of the leptonic branching ratio of the tau (left), which may be enhanced by RPV couplings (right).

handed d-type squark. The DØ collaboration searched for $d\bar{d} \to \tilde{\nu}_\tau \to e\mu$ in 1.0 fb^{-1} of data [5]. The previous search for high-mass resonances decaying into $e\mu$ channel by the CDF collaboration used 344 pb^{-1}[6]. We include the third generation lepton in final states and search for $p\overline{p} \to \tilde{\nu}_\tau \to e\mu/e\tau/\mu\tau$ in 1 fb^{-1} of data collected by CDF to probe the RPV couplings (Figure 2.6).

2.3 Lepton Flavor Violation

In the SM, besides L number, another quantum number, the lepton flavor number, is assigned to the three flavor leptons[4]. The lepton flavor violation interaction (the number of leptons of same flavor not conserved) is not predicted in the SM. For example, the muon decays as $\mu^- \to e^-\bar{\nu}_e\nu_\mu$ where the lepton flavor number L_e and L_μ are conserved, while the interaction of $\mu^- \to e^-\gamma$ is not allowed in the SM.

In the SM, fermions obtain mass by interacting with the Higgs field. These processes involve both left-handed and right-handed fermions. The evidence for neutrino oscillations[5] indicates that the neutrinos have masses. However, the right-handed

[4] $L_e = +1$ for the e and ν_e, $L_e = -1$ for e^+ and $\bar{\nu}_e$. Similar assignment for L_μ and L_τ.

[5] A neutrino created with one flavor is found to change to a different flavor as it travels.

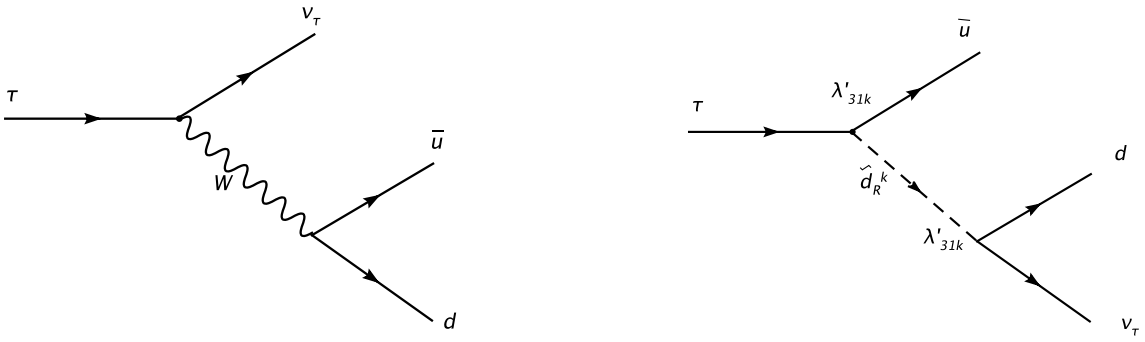

Figure 2.5: **Processes Contributing to the Measurement of λ'_{311}.** The limits on λ'_{311} come from measurements of the hadronic branching ratio of the tau (left), which may be enhanced by RPV couplings (right).

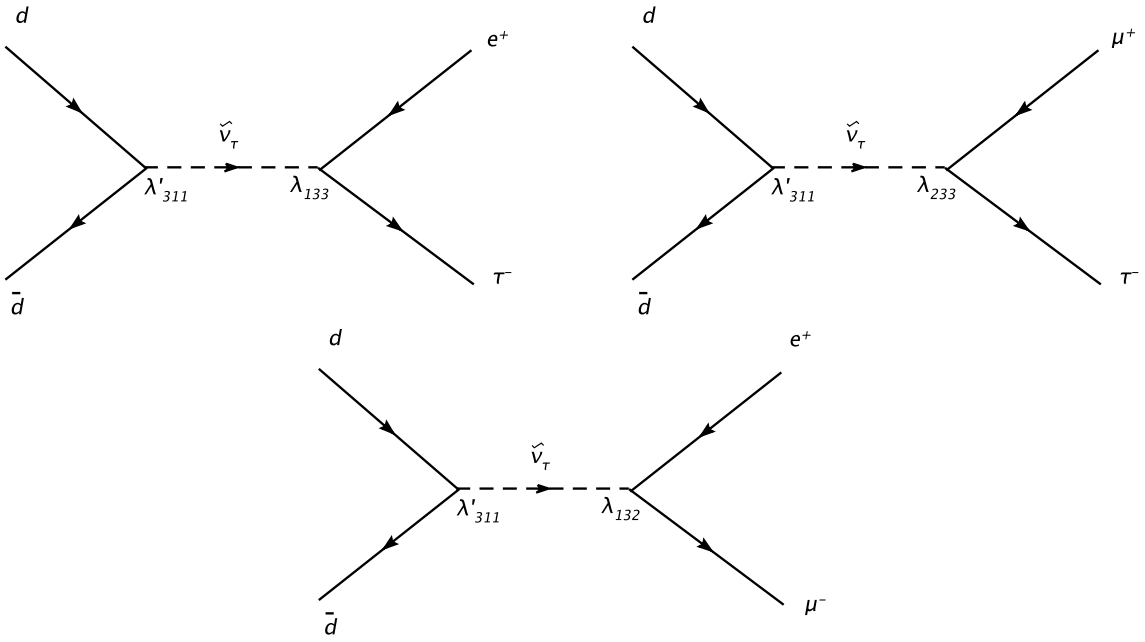

Figure 2.6: **RPV Sneutrino Production and Decay.** Non-zero λ_{133}, λ_{233}, λ_{132} and λ'_{311} make $\widetilde{\nu}_\tau$ produced from $d\bar{d}$ and decaying into $e\tau$, $\mu\tau$ and $e\mu$.

neutrinos have not been observed so far. Therefore, the neutrinos are massless in the SM. To incorporate neutrino masses, several possibilities have been suggested in new physics models. For example, one can obtain the gauge-invariant Dirac mass terms by introducing right-handed neutrinos. However, the Dirac mass terms for neutrinos are difficult to rationalize. The mass of neutrinos from the Dirac term is in the order of $y^D v$, where y^D is the Yukawa coupling and v is the vacuum expectation value of the Higgs. To obtain the neutrino masses with the order of a few eV, y^D needs to be extremely small. It is not natural compared with other Yukawa couplings for the charged leptons. Therefore, the Marojana neutrino mass terms which couple the particle with its anti-particle are more favored than Dirac terms. The Marojana mass terms not only violate L number by a unit of 2, but also potentially violate lepton flavor number[6]. All these facts suggest we should probe lepton flavor violating (LFV) interactions.

The Supersymmetric $U(1)'$ Model With Non-Universal Couplings

In this framework, the SM gauge group with an extra U(1)′ was obtained from breaking gauge group E_6.

$$E_6 \to SU(10) \times U(1)_4 \to SU(5) \times U(1)_\chi \times U(1)_\psi \to SU(3) \times SU(2) \times U(1)_Z \times U(1) \quad (2.3)$$

In SUSY, the supersymmetric Higgs mass parameter μ is the coupling of the superpotential term $\mu H_u H_d$. When electroweak symmetry breaks, both H_u and H_d gets a non-zero vacuum expectation value related to μ. Therefore, the μ parameter should be of the order of magnitude of the electroweak scale. This seems unnatural: why is this scale so much smaller than the Planck scale? It is so called "μ problem". An extra $U(1)'$ can provide a solution to the μ problem because $U(1)'$ symmetry can forbid the μ term in the superpotential. The gauge boson of $U(1)'$ is Z'. The LFV interaction of Z' is allowed and is specified by the Lagrangian density: $\frac{g'_Z}{\sin\theta_W}[\bar{\psi}_i Q^{\psi}_{ij} \gamma^\mu \psi_j] X_\mu$,

[6]The Majorana terms violate the lepton flavor number if the Majorana mass matrix is not diagonal.

E_6 Model	g_x/g_y	Q^l_{12} upper limit	$Q^l_{13}Q^l_{23}$ upper limit
χ	0.335	$10^{-7} - 10^{-5}$	$9 \times 10^{-8} - 9 \times 10^{-6}$
ψ	0.432	$8 \times 10^{-8} - 8 \times 10^{-6}$	$5 \times 10^{-8} - 5 \times 10^{-6}$
η	0.547	$5 \times 10^{-8} - 5 \times 10^{-6}$	$3 \times 10^{-8} - 3 \times 10^{-6}$
Secluded	1.29	$2 \times 10^{-9} - 1 \times 10^{-6}$	$1 \times 10^{-8} - 6 \times 10^{-6}$

Table 2.3: **Limits on Q^l_{ij} from low energy experiment.** The range of the limits are corresponding to the different Z' mass $M_{Z'}$ between 0.1 TeV and 1 TeV

where i, j are generation indices, g'_Z is the $U(1)'$ gauge coupling, $\sin\theta_W$ is electroweak mixing angle and Q^{ψ}_{ij} is referred to as the "charges" [7]. Therefore, Z' produced by $p\bar{p}$ can decay into $e\mu$, $e\tau$ and $\mu\tau$, the same final states that we are interested. The process rates are governed by the lepton charges Q^l_{ij}, while Q^l_{ij} are constrained by low energy experiments. The μ conversion experiment in SINDRUM II at the Paul Scherrer Institute holds the best limit on the ratio of the μ conversion process to weak decays, which is $R_1 = \sigma(\mu^- N \to e^- N)/\sigma(\mu^- N \to \nu^-_\mu N') < 6.1 \times 10^{-13}$ [8]. If Z' is involved in the loop contribution to $\mu^- N \to e^- N$, the ratio R_1 is related to Q^l_{12} by:

$$R_1 = 3.1 \times 10^{-11} \left(\frac{g_x}{g_y}\right)^4 \left(\frac{Q^l_{12}}{10^{-5}}\right)^2 \left(\frac{1\text{TeV}}{m_x}\right)^4 \tag{2.4}$$

where g_x and g_y are the $U(1)'$ and SM $U(1)$ gauge couplings, m_x is the mass of the new gauge boson Z'. Therefore the limits on R_1 can be translated into the limits on Q^l_{12} in E_6 models as in Table 2.3.

The process $\mu^+ \to e^+\gamma$ probes Q^l_{13} and Q^l_{23}. The ratio of the width of $\mu^+ \to e^+\gamma$ to SM process is related to the charges by:

$$R_2 = 1.3 \times 10^{-13} \left(\frac{g_x}{g_y}\right)^4 \left(\frac{Q^l_{13}Q^l_{23}}{10^{-5}}\right)^2 \left(\frac{1\text{TeV}}{m_x}\right)^4 \tag{2.5}$$

The current upper limit of R_2 is 1.2×10^{-11}, which can be translated into the limits on $Q^l_{13}Q^l_{23}$ in E_6 models as in Table 2.3.

The CDF collaboration performed a search for $p\bar{p} \to Z' \to e\mu$ and excluded a region of the Q^l_{12} vs. $M_{Z'}$ space[6]. Although the limit is not competitive with the

result from the low energy experiment, it is still a valuable search because it is a less model dependent direct search.

LFV decays of Higgs

In the case of the two Higgs doublet model (THDM), the LFV interactions of the neutral Higgs boson take the form:

$$\mathcal{L}_{LFV} = \lambda_{ij} \frac{(m_i m_j)^{1/2}}{v} \cos\alpha \bar{l_i} l_j H^0 + h.c. \tag{2.6}$$

which include: $H \to e\mu/e\tau/\mu\tau$.

The current constraints on λ_{23} (< 10) comes from the muon anomalous magnetic moment experiment [9]. The muon magnetic momentum is defined as $\overrightarrow{M} = g_\mu \frac{e}{2m_\mu} \overrightarrow{S}$, where the g-factor predicted by the SM is 2. The difference between the experimentally observed value of the g-factor and the prediction from the SM can be interpreted as the contribution from new physics. In particular, when the contributions from the LFV processes are considered, the LFV coupling λ_{23} are constrained by the muon anomalous magnetic moment experiment results.

Chapter 3

The Accelerator and the CDF Detector

3.1 Accelerator

The Tevatron at Fermilab is a synchrotron, accelerating proton and anti-proton beams to the energy of 0.98 TeV in the 1 km radius superconducting ring. The processes are produced during the collisions at the rate of integrated luminosity $\mathcal{L}_{int}$ $\times$ cross section σ. To study a rare process which usually has very small cross section, a high luminosity is needed. But the increase of luminosity is limited by the collision frequency f, the number of the particles in each beam (N_P, $N_{\overline{p}}$) and the beam size (A) as:

$$\mathcal{L} = f\frac{N_p N_{\overline{p}}}{4\pi A}. \tag{3.1}$$

At present, the highest instantaneous luminosity at Tevatron is 3×10^{32} cm^{-2}s^{-1} and the integrated luminosity with respected to time since Tevatron started to run is 4 fb^{-1}, which means that if a process has the cross section of 1 fb, there will be 4 events produced in the collisions during the total period of Tevatron running.

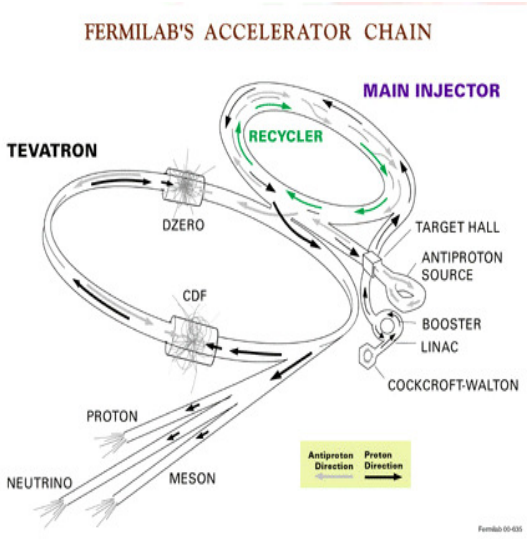

Figure 3.1: **The Fermilab accelerator chain.** It shows the stages in the acceleration of proton and anti-proton, which end with the collision in the Tevatron .

Protons and the antiprotons are produced and accelerated in the Fermilab accelerator chain (Fig.3.1). First, electrons are added to the H atoms to form H^- ions. Then the H^- ions are accelerated to the energy of 750 KeV in the Cockroff-Walton pre-accelerator which is in essence a voltage multiplier generating high voltage at relatively low currents. Then the H^- ions are injected into the 150 m long linear accelerator (Linac). The Linac accelerates the H^- ions to 400 MeV. The electrons are then stripped by passing the ions through a carbon foil. Then the protons are injected to the circular accelerator Booster and are accelerated to the energy of 8 GeV there in a period of 33 ms. The protons from the Booster are injected into the Main Injector. They are accelerated to 120 GeV for the anti-proton production or 150 GeV for injection into the Tevatron. To produce the antipron, 120 GeV protons from the Main Injector interact with a nickel target. Approximately one antiproton is produced for every 10^4 incident protons on the target(Fig. 3.2). After being produced at the target station, antiprotons are sent through the Debuncher. The stochastic cooling system in the Debuncher can reduce the spread in the energy

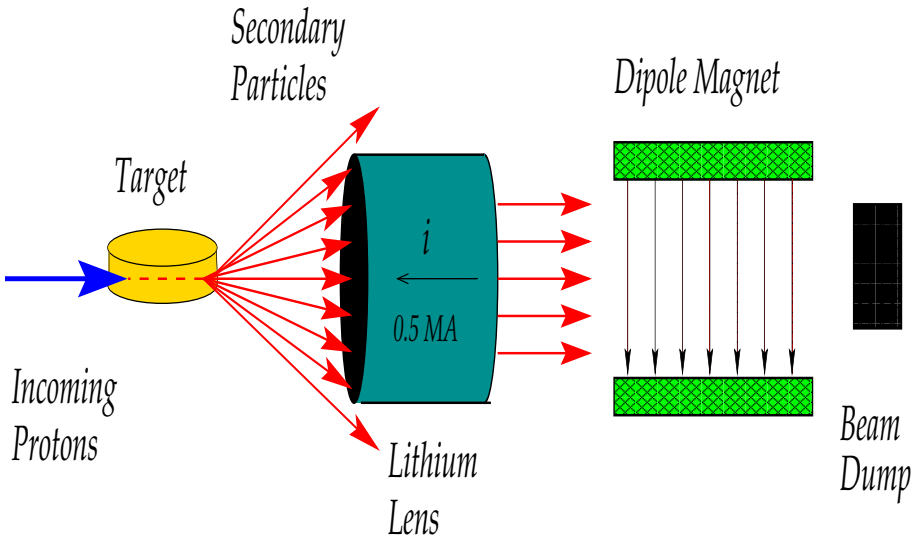

Figure 3.2: **Anti-proton production.** Anti-protons are produced as a beam of protons strikes a nickle target.

distribution of the antiprotons prior to injection the Accumulator. Subsequently, to accumulate a large number of antiprotons, the Accumulator is used to accumulate antiprotons from the Debuncher over several hours or days, where additional cooling systems is necessary to keep the antiprotons at the desired momentum and minimize the transverse beam size. The Recycler ring is a second accumulator ring used to recycle the remaining anti-protons from Tevatron stores. The anti-protons at 8 GeV from either the Accumulator or the Recycler are accelerated to 150 GeV in the Main Injector and then injected into the Tevatron. In the Tevatron, the 3 trains of proton and anti-proton (12 bunches per train, each bunch separated by 396 ns) are accelerated to the energy of 0.98 TeV and collide at the location of the CDF and D0 detectors,

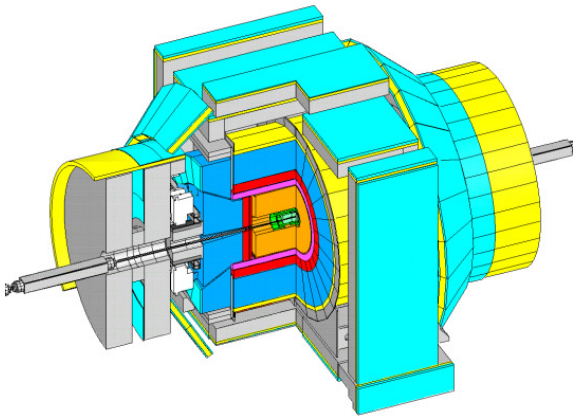

Figure 3.3: **The CDF detector.** The CDF detector is build of several subdetectors that contribute to the reconstruction of physics processes in collisions.

3.2 The CDF Detector

CDF is a general purpose detector, which consists the several of sub-detectors surrounding the interaction area. It is designed to measure the energy, momentum and the identity of particles produced in Tevatron collisions. Starting from the interaction point, particles go through in sequence: the tracking system, calorimeter system and muon system, as shown in Fig 3.3.

3.2.1 The CDF Coordinate System

The CDF detector uses a coordinate system where the $+z$ is the direction along the protons beam, $+x$ is towards the outside of the Tevatron ring and $+y$ is the vertical direction pointing upwards. A cylindrical coordinate system is frequently used: r is the radial distance from the beam line, θ is the polar angle from the beam line ($\theta = 0$ in the direction of $+z$ and $\theta = 90°$ perpendicular to the beam), and ϕ is the azimuthal angle ($\phi = 0$ in the direction of $+x$ and $\phi = 180°$ in the direction of $-x$). In addition, the quantity pseudorapidity η is frequently used, where $\eta = -\ln \tan \frac{\theta}{2}$.

3.3 Tracking System

The CDF Tracking System is designed to reconstruct the trajectories of charged particles. The system, consisting of the Silicon Detectors and the Central Outer Tracker (COT), is contained in a superconducting solenoid which generates a 1.4 T magnetic field parallel to the beam axis.

3.3.1 Silicon Detectors

The CDF silicon detectors are designed for performing secondary vertex measurement and high precision tracking. They consist of 7 central layers (8 forward layers) of silicon microstrip sensors. The sub-detectors include Layer 00, the Silicon Vertex Detector (SVX II) and Intermediate Silicon Layers (ISL). Layer 00, located on the beam pipe at radius $r = 1.35$ cm, consists of single-sided silicon sensors and covers $|\eta| < 4.0$. SVX II, located outside of the Layer 00 at the radius from $r = 2.1$ cm to 17.3 cm, consists of 5 double-sided sensors and covers $|\eta| < 2.0$. The ISL, located between the SVX II and the COT consists of the central layer (at $r = 22$ cm, $|\eta| < 1.0$) and forward layers from $r = 20$ cm to $r = 28$ cm, $1.0 < |\eta| < 2.0$. The r-z plan view of the silicon detectors is show in Fig. 3.4.

When charged particles pass through the silicon sensor, they ionize the silicon and produce electron-hole pairs, the number of which is proportional to the energy loss of the charged particles. Under an external applied electric field, electrons drift towards the anode and holes drift to the cathode, and the charge is collected. The total charge generated by the incident particle is a measure of the deposited energy. The track of the charged particle is reconstructed using the readout information from many sensors. One of advantages of using silicon detectors is the low energy required to create an electron-hole pair, 3.6 eV, less than the ionizing energy in a gas. In addition, the high density of silicon enables precise position measurements (the CDF silicon detector has spacial resolution of 10 μm).

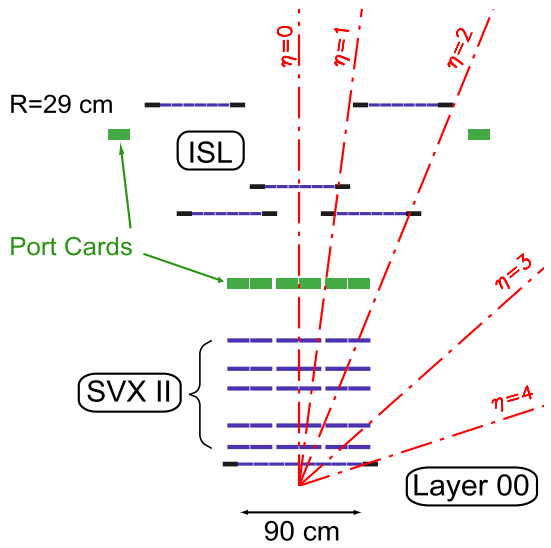

Figure 3.4: **The r-z plan view of the silicon detectors.** The CDF silicon detectors are designed for performing secondary vertex measurement and high precision tracking. They consist of 7 central layers (8 forward layers) of silicon microstrip sensors.

3.3.2 Central Outer Tracker

The Central Outer Tracker (COT) is a cylindrical drift chamber located outside of the Silicon Detectors at a radius from $r = 40$ cm to 137 cm and covers $|\eta| \leq 2.0$. It consists of 8 superlayers (4 in the direction of beam line are called axial superlayers and 4 with stereo angle $\pm 2^\circ$ are called stereo superlayers.) Superlayers are made of varied number of cells (superlayer 1 has 168 cells and superlayer 8 has 480 cells). Each cell consists of a field sheet and 12 sense wires alternated with the potential wires. The chamber is filled with a mixture of Argon and Ethane gas (50 : 50).

A particle passing through the COT interacts with the gas. The molecules are excited and ionized. Positively charged ions and free electrons are created. If a static electric field is applied in the detector, electrons drift in regions of low electric field, then reach the high field or avalanche region near a anode wire, where amplification and detection occur. Electrons drift faster than ions due to their low mass. The drift

velocity also depends on the strength of electric field, the properties of gas molecules , etc.. The drift time, a measure of the position of the original particle, is determined by the drift velocity and the distance.

The COT is used to measure the momentum of the charged particles. The COT is placed in the 1.4 T magnetic field such that the charged particles travel in a helix with the radius $r = \frac{p_T}{|q|B}$, where the $p_T = \sqrt{p_x^2 + p_y^2}$ (transverse momentum), q is the particle charge and B is the magnetic field. By reconstructing the track's curvature in r-ϕ plan, p_T is determined.

3.4 Time of Flight System

The Time of Flight (TOF) is a scintillator detector positioned outside the COT at the radius 1.4 m. It is used for particle identification, especially for distinguishing $K^{\pm}$ from $\pi^{\pm}$, which is very important in B physics. It measures the time of flight of a particle with respect to the collision time. The mass of particles can be determined by $m = \frac{p}{c}\sqrt{\frac{c^2t^2}{L^2} - 1}$, where p is the momentum, L is the path length and t is the time of flight. The TOF allows a 2σ separation of $K^{\pm}$ from $\pi^{\pm}$ with the momentum less than 1.6 GeV/c.

3.5 Calorimeter System

The Calorimeter System, located outside the Tracking System, measures the energy and direction of the particles going out of the tracking system. Covering a pseudo-rapadity range $|\eta| < 3.6$, the whole system consists of Central Calorimeter and Plug Calorimeter, both with electromagnetic and hadronic compartments for measuring the energy of electrons/photons and hadrons respectively.

3.5.1 Central Calorimeter

The Central Calorimeter, segmented into towers (each tower is 15° in azimuthal and 0.11 in pseudorapidity), consists of the Central Electromagnetic Calorimeter(CEM) ($|\eta| < 1.1$), made of lead-scintillator, followed by the Central Hadronic Calorimeter (CHA $|\eta| < 0.9$) and the Endwall Hadronic Calorimeter (WHA $0.8 < |\eta| < 1.2$), made of iron-scintillator.

When the particles (e.g. photon, electron, hadron) pass through the calorimeter, they interact with the material in the calorimeter (lead in the CEM or iron in the CHA) by electromagnetic interactions (in the CEM) or hadronic interactions (in the CHA). Showers of charged particles are produced, where their energies are measured to determine information about the primary particle. The length scale of the shower is set by the radiation length of the material (or the interaction length in case of the hadronic interaction).

The way to measure the energy of hadronic or electromagnetic showers in lead or iron is to place the scintillator next to the lead or iron so that the scintillator emits low-energy photons (blue light) when struck by charged particles from the shower. The produced photons are subsequently collected by photomultiplier tubes (PMTs). By adding up the signal collected in the surrounding photomultiplier tubes, we can determine the energy of the charged particles, therefore the energy of the primary particle. The energy resolution is $13.5\%/\sqrt{E_T} \oplus 2\%$ for CEM ($50\%/\sqrt{E_T} \oplus 3\%$ for the CHA), which is limited by the granularity of the calorimeter.

3.5.2 Calibration of the Electromagnetic ShowerMax Chamber

The CES is a subdetector system which is a multiwire proportional chamber with the 2-coordinate readout (in the strip and wire). An e or γ creates a shower which is read out as two independent clusters: one cluster in the wire direction (parallel

with the proton beam) and one cluster in the strip direction (perpendicular to the beam). The electron reconstruction requires two readout clusters from a strip and wire matching with a COT track. The γ reconstruction requires that no COT track points to the clusters.

Ideally, the energy measurement of the strip cluster and wire cluster from the same shower should be consistent. However, geometry distortions of wires can cause non-uniform gas gap between them. As a result, the ratio R_{sw} becomes a function of the shower position and can vary as much as $\sim 40\%$. A uniform detector response is achieved by determining a global CES energy scale such that the corrected energy of the cluster does not depend on its position.

As a result of calibration, the energy of the strip cluster and the wire cluster from the same e or γ shower would be the same within an accuracy $\sim 5\%$, which significantly increases the efficiency of matching the clusters to form a shower. The e and γ reconstruction benefit from the calibration mentioned above.

3.5.3 Plug Calorimeter

To extend the coverage of the calorimeter to a larger pseudorapidity, the Plug Electromagnetic Calorimeter (PEM) was placed outside the barrel end of COT (one plug on each side, which covers $1.1 < |\eta| < 3.6$) and the Plug Hadronic Calorimeter (PHA) follows the PEM, covering $1.2 < |\eta| < 3.6$).

3.6 Muon System

The Muon System is the outermost device, located outside the Calorimeter System. Because muons don't interact strongly with matter and have a long life time (2.2 μsec), they can travel a long distance, pass through the calorimeters, and reach the muon detectors. Muon detection has low background because in general other charged particles have been absorbed before reaching the muon detectors. The Muon

System at CDF consists 4 sub-detectors: Central Muon Detector (CMU $|\eta| < 0.6$), Central Muon Upgrade (CMP $|\eta| < 0.6$), Central Muon Extension (CMX $0.6 < |\eta| < 1.0$) and Barrel Muon Detector (BMU $1.0 < |\eta| < 1.5$). They are made of single wire drift chambers.

When a muon reaches the Muon Detectors, it interacts with the gas in the drift chamber, which produces electrons drifting in the electric field that are collected by the anode wire (similar mechanism to the COT). The existence of the muon stub, which is reconstructed from the hits, in the muon detectors is the main criteria for muon identification.

3.7 Trigger

Given that among the large number of events produced in collisions only very few are interesting physics events, the CDF trigger system is designed to rapidly decide which events to keep, when only a small fraction of the total can be recorded. The CDF 3 Level trigger system reduces the event rate of ~ 2.5 MHz down to ~ 100 Hz for data storage and off-line analysis.

Level 1 (L1): a hardware trigger which uses the information from the readout electronics of the sub-detectors and make a decision by simply counting the physics object (e.g. one 8 GeV electron). The time between the bunch crossing and the decision being made by the L1 is less than 5 μsec. The output event rate is ~ 30 kHz.

Level 2 (L2): the events accepted by L1 are sent to one out of four L2 buffers for partially reconstructing and evaluating (up to 4 events can be processed at the same time). The time for processing is up to 35 μsec per event. The output event rate of the L2 is ~ 1 kHz.

Level 3 (L3): L3 accesses the complete information of the event and uses the offline code (tracking, calorimeter, muon stub finding algorithm, etc.) to reconstruct

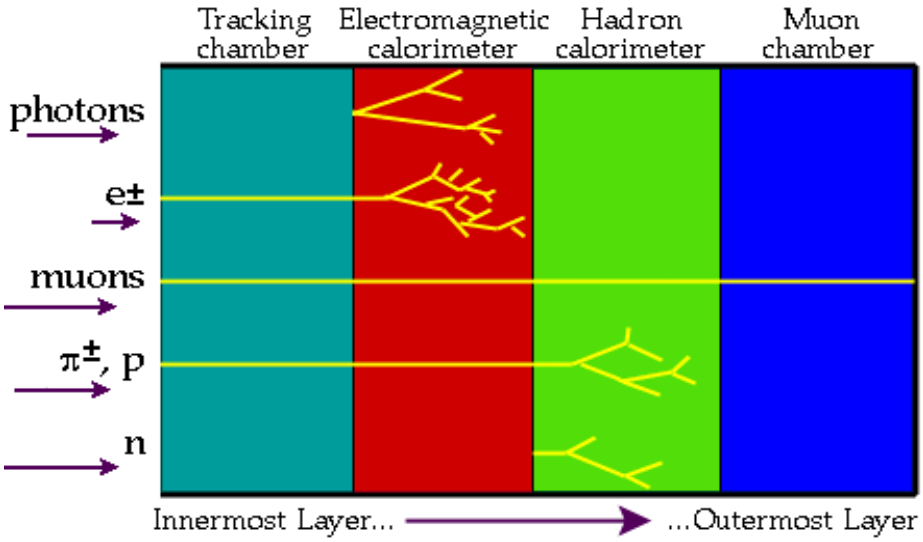

Figure 3.5: **The behaviors of various particles in the CDF detector.**

and select the events being accepted by the L1 and L2. The reconstruction and selection are performed by a farm of Linux PC's such the processing time per event is of the order of one second. L3 further reduce the event rate to $\sim$ 100 Hz.

3.8 Production Algorithm

The events passing the L3 trigger are recorded to tapes. To determine the initial physical process occurring at the interaction point, we need to reconstruct the event in a more precise way compared to the trigger level. At CDF, we have two stages for reconstructing the events off-line. First, we pass the event information from the subdetectors to the production algorithms (particles produced in the physical process are detected by the subdetectors as shown in Figure 3.5.), which reconstruct the basic objects such as electromagnetic clusters, tau candidates and muon candidates. Second, the basic objects reconstructed by the production algorithm need to pass some identification criteria, to be identified as real physical particles. The lepton identification algorithms will be described in the next chapter.

Chapter 4

Lepton Identification

In this analysis, we are searching for the signatures with full lepton final states. Therefore, efficient lepton identification algorithms are required to fully reconstruct the physics events. In this Chapter, we will describe the electron, muon and tau identification algorithms, which identify the basic objects, electromagnetic clusters, tau candidates and muon candidates that are reconstructed by the production algorithm. In particular, we will describe the improvements on electron and tau identification algorithms, compared with the CDF default algorithm.

4.1 Electron

Electron reconstruction starts from a cluster of energy in the central calorimeter, matching it to a shower in the CES and a COT track. To obtain a pure sample of electrons, a set of identification criteria is then applied to the electron candidates. Based on the new CES calibration (described in 3.5.2), which gives more robust track-CES matching, we have developed a new set of electron identification criteria, where we inherit some standard electron identification criteria and modify those less efficient criteria.

The criteria inherited from the CDF standard electron identification are the following:

Geometric and kinematic requirements: the electron is required to be in the central region, with pseudorapidity $|\eta|$ less than 1.0. The track must extrapolate into the fiducial region of CES. We require a transverse energy E_T greater than 20 GeV and a transverse momentum P_T greater than 10 GeV/c, because we consider only high E_T electrons. The track must originate from the beam spot. The distance between the electron track and the interaction point in the z-coordinate Z_0 must be less than 60 cm.

Track quality requirements: the electron track is required to have more than 3 axial (stereo) COT segments with at least 5 hits each. The χ^2/dof, chi square divided by the number of degrees of freedom, which reflects the goodness of the fit to hits in COT track reconstruction, needs to be less than 3.

Other requirements: we require that the electron is not from a γ conversion [11]. The basic idea of the conversion rejection algorithm is to reject an electron accompanied by a opposite-sign track which originates from the same displaced point. Because a real electron deposits most of its energy in the electromagnetic calorimeter, we require the ratio of the total hadronic energy over the total electromagnetic energy of the shower, E_{had}/E_{em}, to be less than $0.055+0.00045\times E$. To isolate the electron from background, the isolation energy defined as the measured energy surrounding the electron (within the cone $R \leq 0.4$, where $R = \sqrt{\eta^2 + \phi^2}$) is required to be less than 10% of the electron energy. The Lshr (Lateral Shower Sharing) variable is used to compare the energy deposition in the adjacent tower (next to the seed tower, the most energetic one) with the expected value from the test beam electron shower. Its definition is

Lshr $= 0.14\frac{\Sigma_i(E_i^{measure}-E_i^{expect})}{\sqrt{(0.014\sqrt{E_{EM}})^2+\sum_i(\Delta E_i^{expect})^2}}$, where $E_i^{measure}$ is the the energy measured in the i*th* adjacent tower, E_i^{expect} is the expected energy, $0.014\sqrt{E_{EM}}$ is the uncertainty of the EM energy measurement and ΔE_i^{expect} is the uncertainty of the expected energy.

Modification to standard electron identification as used in the new identification are:

$E/P_{track} \leq 2$**:** the standard $E/P_{track} \leq 2$ criteria is designed to reject electron originating from γ conversion. However, it also suppresses electrons that bremsstrahlung. When an electron radiates a γ, the momentum of the electron track decreases but the total energy assigned to the electron does not since the γ close to the electron is detected in calorimeter and contributes to the electron energy measurement. Therefore an electron experiencing bremsstrahlung exhibits $E/P_{track} \geq 2$. To recover this kind of electron, we remove the E/P cut and rely on explicit conversion removal, since the CES calibration helps resolve the overlapped clusters from converted electrons more efficiently.

$-3.0 \leq Q \cdot \Delta X \leq 1.5$ **and** $|\Delta Z_{ces}| \leq 3.0$ cm**:** the ΔX_{ces} and ΔZ_{ces} are distances between the track extrapolated to the plane of the CES and the shower position measured by the CES (in x and z coordinates). A good match between the cluster and the track is required. We remove these 1-dimensional cuts and replace them by a 2-dimensional cut (described later).

$\chi^2_{strip} \leq 10$**:** this requirement is applied to compare the profile of the CES strip cluster with respect to the cluster shape from electron test beam data. We remove this cut because the reconstruction of the CES clusters is more reliable after we have calibrated the CES energy response.

The new identification criteria:

	CDF Default "tight" CEM	New "tight" CEM
DetCode	= 0(central)	= 0(central)
FidEleTrk	= 4	= 4
|ZCot|		$\leq$ 155 cm
ZCes	9 cm $\sim$ 230 cm	9 cm $\sim$ 230 cm
|XCes|	$\leq$ 21.5 cm	$\leq$ 21.5 *cm*
E_T	$\geq$ 20 GeV	$\geq$ 20 GeV
Beam constrained P_T	$\geq$ 10 GeV/c	$\geq$ 10 GeV/c
Beam constrained $\|Z_0\|$	$\leq$ 60.0 cm	$\leq$ 60.0 cm
COT Ax. Seg.	$\geq$ 3 (5)	$\geq$ 3 (5)
COT St. Seg.	$\geq$ 3 (5)	$\geq$ 3 (5)
χ^2_{cot}	$\leq$ 3	$\leq$ 3
Conversion	false	false
E_{had}/E_{em}	$\leq 0.055 + 0.00045 * E$	$\leq 0.055 + 0.00045 *$ E
Isolation	$\leq$ 0.1	$\leq$ 0.1
Lshr	$\leq$ 0.2	$\leq$ 0.2
E/P_{track}	$\leq$ 2 unless $P_T \geq$ 50GeV	
$Q \cdot \Delta X_{ces}$	$-3.0 \leq Q \cdot \Delta X \leq 1.5$	
$\|\Delta Z_{ces}\|$	$\leq$ 3.0 cm	
χ^2_{strip}	$\leq$ 10	
ΔR_{ces}		$\leq$ 3.0 cm
E_{ces}/P_{track}		$\geq$ 0.3

Table 4.1: **List of Electron Identification Criteria.**

$\Delta R_{ces} \leq 3.0$ **cm:** we cut on the 2-D distance between the extrapolated track and the CES shower, instead of cutting on 1-D distances ΔX_{CES} and ΔZ_{CES},.

$E_{ces}/P_{track} \geq 0.3$**:** we require the energy of the CES shower E_{ces} to be consistent with the track momentum P_{track}.

The electron identification criteria are summarized as in Table 4.1.

4.1.1 Electron identification Efficiency ϵ_{ele} and Scale Factor

Electron identification efficiency is the probability for electron candidates to pass the identification selection.

We measure the electron identification efficiency in data ($\epsilon_{\rm ele}^{\rm data}$) and Monte Carlo generated sample ($\epsilon_{\rm ele}^{\rm MC}$). The ratio of $\epsilon_{\rm ele}^{\rm data}$ and $\epsilon_{\rm ele}^{\rm MC}$ is referred to as the scale factor, which can be used to rescale the $\epsilon_{\rm ele}^{\rm MC}$.

We use $Z \rightarrow e^+e^-$ events to measure the $\epsilon_{\rm ID}$. To select $Z \rightarrow e^+e^-$ events, we require one isolated central electron passing all the tight cuts listed in Table 4.1 and another central electron passing all the probe cuts (which are geometric and kinematic cuts). In addition, the two electrons are required to have opposite charge and invariant mass are in the range 76 GeV/c^2 $<$ M$_{\rm ee}$ $<$ 106 GeV/c^2.

The identification efficiency is calculated as:

$$\epsilon_{\rm ele} = \frac{2{\rm N_{TT}}}{{\rm N_{TP}} + {\rm N_{TT}}} \tag{4.1}$$

where $\rm N_{TP}$ is the number of events with one tight electron and one probe electron and $\rm N_{TT}$ is the number of events with two tight electrons.

The selected events in data contain QCD dijets and γ+jets background. We measure the background using the events which contain two leptons with the same charge (referred to as "same sign" events), because the probability of finding "same sign" electron pairs and "opposite sign" pairs are the same in the background events. We need to take into account that "trident" Z $\rightarrow$ e$^+$e$^-$ events (where one of the electrons radiates a γ which converts into e^+e^-) could also yield same sign electron pairs. We use a Monte Carlo generated sample to estimate the number of same sign events from trident events. Then we subtract them from the total same sign events in data as an estimate of background in data.

	Monte Carlo generated sample	data
$\rm N_{TP(opposite\ sign)}$	133757	8582
$\rm N_{TP(same\ sign)}$	1246 (trident)	169
$\rm N_{TP(corrected\ same\ sign)}$	–	89
$\rm N_{TT(opposite\ sign)}$	113380	7051
$\rm N_{TT(same\ sign)}$	163 (trident)	16
$\rm N_{TT(corrected\ same\ sign)}$	–	6

The identification efficiency measured in the Monte Carlo generated sample is:

$$\epsilon_{\rm ele}^{\rm MC} = \frac{2 \times (113380)}{133757 + 113380} = 91.8\% \tag{4.2}$$

and in data:

$$\epsilon_{\rm ele}^{\rm data} = \frac{2 \times (7051 - 6)}{(8582 - 89) + (7051 - 6)} = 90.7\% \tag{4.3}$$

The scale factor between data and Monte Carlo generated sample is $\epsilon_{\rm ele}^{\rm data}/\epsilon_{\rm ele}^{\rm MC} = 90.7\%/91.8\% = 0.99$

4.1.2 Jet-to-Electron Misidentification Probability

Hadrons from quark and gluon fragmentation are reconstructed as jets. Some of hadronic jets deposit more energy in the electromagnetic calorimeter and appear like electrons. For instance, a $\pi^+\pi^0$ jet system might be reconstructed as an electron candidate.

To study the probability for those electron candidates from jets to be misidentified as electrons, we use the following triggered data samples: Jet20, Jet50, Jet70, Jet100 (at least one jet with $\rm E_T > 20,\ 50,\ 70,\ 100$ GeV, reconstructed in a cone, $\Delta \rm R \leq 0.7$, where $\Delta \rm R = \sqrt{\Delta\eta^2 + \Delta\phi^2}$); and Monte Carlo generated samples Jet300 (Jet500), which are generated with at least one parton with $\rm P_T > 300$ GeV/c ($\rm P_T > 500$ GeV/c). The jet-to-electron misidentification probability is defined as:

$$\rm P_{mis}^{ele} = \frac{N_{tight}}{N_{candidates}} \tag{4.4}$$

where $\rm N_{candidates}$ is the number of the electron candidates with $\rm E_T > 20$ GeV in the Jet20 sample ($>$ 50 GeV in Jet50 sample, etc.), track $\rm P_T > 10$ GeV/c, $\frac{\rm HadEt}{\rm EmEt} < 0.06 + 0.006 \times \rm E$ in the jet sample, $\rm N_{tight}$ is the number of denominator candidates passing the tight electron identification selection. We measure $\rm P_{mis}^{ele}$ as a function of electron energy. We found that $\rm P_{mis}^{ele}$ in different jet samples are consistent within the statistical uncertainty. The $\rm P_{mis}^{ele}$ in the Monte Carlo generated samples are consistent with the extrapolation from the data, shown in Figure 4.1.

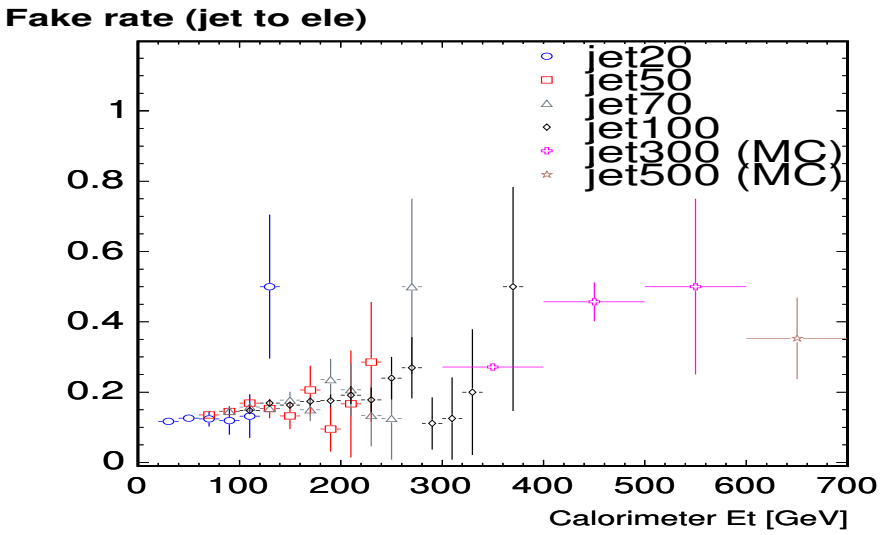

Figure 4.1: **Jet-to-Electron Misidentification Probability.** We found that the misidentification probability in different samples are consistent within the statistical uncertainty. The misidentification probability in the Monte Carlo generated samples are consistent with the extrapolation from the data.

4.2 Muon

A muon is reconstructed by matching the stub in the muon detectors to a COT track. In this analysis, we require that muons either have the CMU-only stubs, CMP-only stubs, CMU and CMP stubs or CMX stubs. They are required to pass the standard CDF muon identification cuts listed in Table 4.2.

4.3 Tau

Taus require special selection criteria, being heavy ($m_\tau = 1.777$ GeV/c^2) and unstable ($c\tau = 87$ μm). We know that 35% of taus decay leptonically to $\ell\nu_\tau\nu_\ell(\gamma)$ where $\ell = e,\ \mu$ and 65% of taus decay hadronicly into hadrons plus ν_τ. In this analysis, we can only use the hadronic decay modes of the tau in order to distinguish taus from the prompt electron and muon in the final states, where the the hadronic taus

	Muon identification
Beam constrained P_T	≥ 20 GeV
Beam constrained $\lvert Z_0 \rvert$	≤ 60.0 cm
E_{Had}	$\leq \max(6, 6 + 0.0280 \times (P - 100))$ GeV
E_{Em}	$\leq \max(2, 2 + 0.0115 \times (P - 100))$ GeV
χ^2_{cot}	≤ 3
COT Ax. Seg.	$\geq 3(5)$
COT St. Seg.	$\geq 3(5)$
Track $\lvert D_0 \rvert$	≤ 0.2 cm if no silicon hits
Track $\lvert D_0 \rvert$	≤ 0.02 cm if silicon hits > 0
Track Isolation	≤ 0.1
ΔX_{cmu}	≤ 3.0 cm
ΔX_{cmp}	≤ 6.0 cm
ΔX_{cmx}	≤ 6.0 cm if CMX
$\rho(\eta, Z_0, 155)$	≥ 140 cm if CMX

Table 4.2: **List of Muon Identification Criteria.**

have a less accurate energy measurement, lower identification efficiency and higher background compared to the other charged leptons. In order to increase the signal acceptance and reduce the background in tau channels, we have made several improvements in this work. First, we improves the accuracy of the reconstructed tau energy based on the calibration of CES energy response. We develop new algorithms to reduce the background due to the misidentification. Finally, we have improved some tau identification criteria, which had been used as the default at CDF but were found less efficient for the energetic taus from heavy particles decay.

We reconstruct hadronic taus through their decay products, π^0, $\pi^\pm$ and $K^\pm$ by using tracks in the COT, energy clusters in the calorimeter, and CES information. The ν_τ escapes from the detector and contributes to the missing transverse energy (MET).

A new tau cluster is reconstructed starting from a seed tower, which is required to have $E_T > 6$ GeV. All the neighboring towers are added to the cluster if their $E_T > 1$ GeV. Given the tau mass, the size of the cluster is expected to be small.

Therefore, we require the tau cluster to have ≤ 6 towers.

To reconstruct tracks produced by the charged particles from tau decays, all the COT tracks are extrapolated to the calorimeter. The highest P_T track that falls within a cone $\Delta R \leq 0.4$ around the cluster is chosen as the seed track of the tau. The seed track is required to have transverse momentum $P_T > 4.5$ GeV/c. There may be more than one charged track produced in hadronic tau decays, so the tracks with $P_T > 1$ GeV/c and within 10 degrees around the seed track are added as tau tracks.

The π^0 is reconstructed by its decay products, $\gamma\gamma$. The standard CDF π^0 reconstruction algorithm measures the shower position using the CES and the energy from CEM. However, when the π^0 is from a tau decay, it is frequently accompanied by charged $\pi^{\pm}$('s) or $K^{\pm}$('s), which sometimes also deposit energy in CEM. This affects the accuracy of the energy measurement of the π^0 from the CEM. However, the charged $\pi^{\pm}$ and $K^{\pm}$ behave as minimum ionizing particles in the CES because the CES is located in the front part of the CEM. In addition we can distinguish the charged $\pi^{\pm}$ and $K^{\pm}$ from π^0 through their different shower profiles in the CES. Therefore, we can use the calibrated CES instead of the CEM to measure the π^0 energy with better accuracy.

Besides, in the CDF standard algorithm we fail to reconstruct a π^0 if the π^0 is very close to a track (distance < 4 cm). A large discrepancy ($> 3\sigma$) between the CEM energy measurement of tau and the tau visible energy (the energy of visible four-momentum — sum of the tau track and π^0 four-momenta) would indicate that the π^0 is missing. To recover the missed π^0, we assign a neutral particle with the energy equal to $E_{CEM} - E_{visible}$ and associate it to the tau.

As a result of the improvements mentioned above, the resolution of the tau visible energy improves as shown in Figure 4.2.

In order to identify a tau, besides the geometric, kinematic and track quality cuts, the following tau identification cuts are applied:

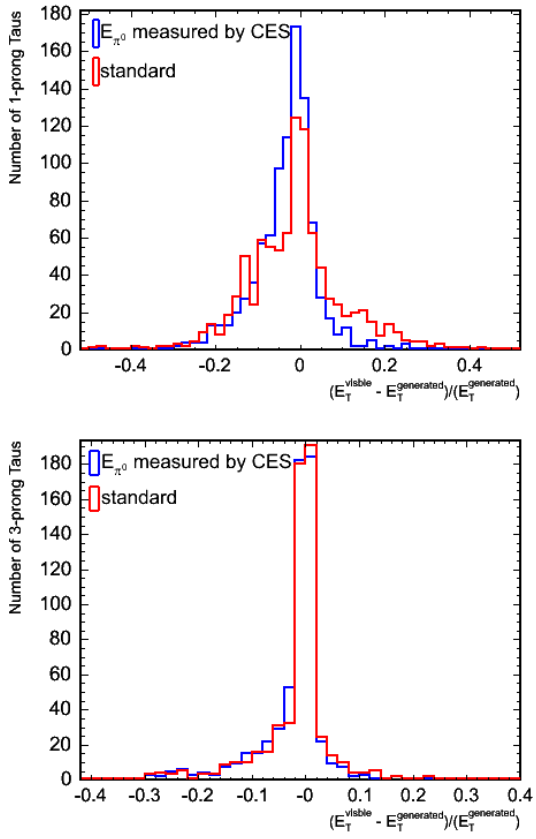

Figure 4.2: **Tau Visible Energy Measurement.** Reconstructed tau visible energy is closer to the real energy (at generator level in Monte Carlo generated samples) using the new algorithm (blue) compared to the CDF default reconstruction algorithm (red).

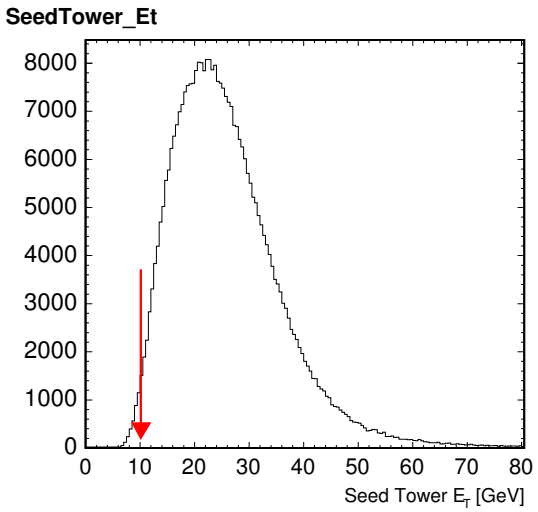

Figure 4.3: **Tau Seed Tower** E_T**.** The seed tower E_T distribution of taus from W boson decays (Monte Carlo generated sample).

seed tower $E_T \geq 10$ GeV**:** the seed tower is the highest E_T calorimeter tower. The cut value is selected because most taus from heavy particle decays have a seed tower $E_T > 10$ GeV. Figure 4.3 shows the seed tower E_T distribution of taus from W boson decays in a Monte Carlo sample.

seed track impact parameter $|D_0| \leq 0.2$ cm**:** the seed track impact parameter $|D_0|$ is the minimum distance from the interaction point in the transverse plane. Figure 4.4 shows the seed track D_0 distribution for taus from W boson decays in a Monte Carlo sample.

track isolation: tracks are not allowed within the isolation annulus, where the annulus is between θ_{sig} (10°) and θ_{iso} (30°) surrounding the seed track, given that tau jet is narrow, as shown in Figure 4.5.

There are three new criteria to improve the tau identification. They are electron

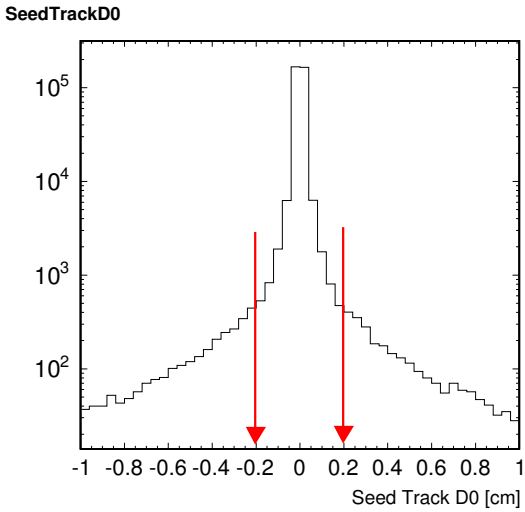

Figure 4.4: **Tau Seed Track Impact Parameter.** The seed track impact parameter D_0 distribution of taus from W boson decaying (Monte Carlo generated sample).

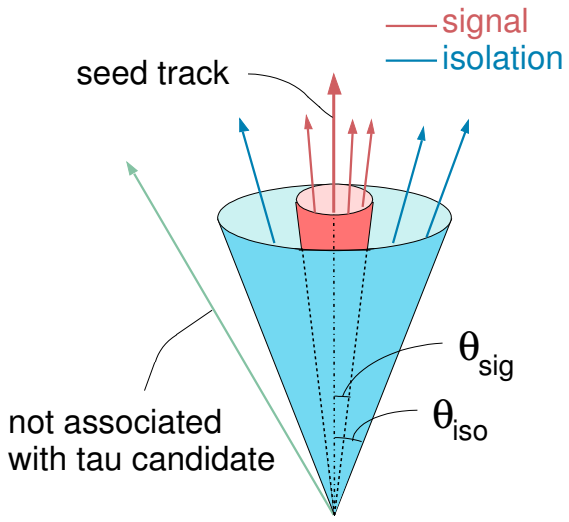

Figure 4.5: **Tau Isolation Annulus.** Tracks are not allowed within the isolation annulus (between θ_{sig} and θ_{iso}).

removal, muon removal and energy dependent mass selection, which will be described in the following discussions respectively.

First, electrons are easily confused with those taus which have one track plus a π^0. In fact, almost every high-P_T electron can be misreconstructed as a tau candidate. We somehow have to reject these false taus. The standard CDF approach requires $\frac{E_{EM}}{E_{total}} < 1 - \frac{\xi}{E/P}$, where EM fraction $\frac{E_{EM}}{E_{total}}$ is the ratio of electromagnetic energy to total energy, E/P is the ratio of energy to momentum of the tau, and ξ is a constant. The ξ-based cut is applied because electrons have large EM fraction. However, sometimes real taus could also exhibit large EM fraction, as shown in Figure 4.6, where $\xi = 0.2$, and Figure 4.7. So not only electrons, also about 10% of real taus are rejected by the ξ-based cut. In addition, the rejection power of the ξ-based cut decreases for high energy electrons, because they have a larger energy leakage in the hadronic calorimeter, therefore the EM fraction is smaller.

We developed a new algorithm, which explicitly identifies electrons to be rejected using more information. To do that, for each reconstructed tau candidate we build a corresponding electron object by converting the variables associated with the tau candidate into electron variables and calculate χ^2_{ele} as

$$\chi^2_{ele} = \frac{(1 - \frac{E_{EM}}{E_{total}})^2}{\sigma^2_{EM}} + \frac{\Delta X_{CES}{}^2}{\sigma^2_{X_{CES}}} + \frac{(1 - E_{CES}/P)^2}{\sigma^2_{EP}} \tag{4.5}$$

where σ_{EM} is the peak width of the $\frac{E_{EM}}{E_{total}}$ distribution, $\sigma_{X_{CES}}$ is the space resolution of CES, and σ_{EP} is the peak width of the $\frac{E_{CES}}{P}$ distribution. The first term requires the EM fraction to be close one. The second term requires the residual between the track and the nearby CES shower to be small. The last term requires the energy of the reconstructed CES shower, E_{CES} to be consistent with the track momentum P. If the electron object has $\chi^2_{ele} < 10$ and passes all the "loose" electron identification cuts listed in Table 4.3, it is considered to be consistent with a real electron and is rejected. Figure 4.8 shows the invariant mass formed from electron and tau candidates reconstructed in the $Z \to ee$ Monte Carlo sample, where tau candidates are actually from the electron produced in Z decay. From the figure, we can see

	"loose" CEM
DetCode	=0(central)
FidEleTrk	=4
|ZCot|	$\leq$ 155 cm
ZCes	9 cm $\sim$ 230 cm
E_T	$\geq$ 10 GeV
Beam constrained P_T	$\geq$ 5 GeV/c
Beam constrained $\|Z_0\|$	$\leq$ 60.0 cm
COT Ax. Seg.	$\geq$ 3 (5)
COT St. Seg.	$\geq$ 3 (5)
χ^2_{cot}	$\leq$ 3
E_{had}/E_{em}	$\leq 0.06 + 0.0006 * E$
Isolation	$\leq$ 0.2
$\|DeltaX_{ces}\|$	$\leq$ 3.0 cm (if $X_{ces} \leq 21.5$)
$\|\Delta Z_{ces}\|$	$\leq$ 3.0 cm (if $X_{ces} \leq 21.5$)
E_{ces}/P_{track}	$\geq$ 0.2
χ^2_{ele}	$\geq$ 10

Table 4.3: **List of "Loose" Electron Identification Criteria.**

that we have rejected most misidentified tau candidates coming from the electrons by applying the electron removal criteria.

In addition to rejecting electrons, we also need to reject the misreconstructed tau candidates from muons. Most muons are very distinguishable from taus because they behave as minimum ionizing particles in the calorimeter, failing the $E_T > 20$ GeV cut in tau identification. However, some muons interact in the calorimeter or radiate a γ, which deposits a significant amount of energy in the calorimeter. These muons can pass tau identification cuts and mimic taus. In the CDF default tau identification, there is no muon removal cut to remove this kind of muon. In the new identification, we add a cut to reject them. We reject the tau candidate if it overlaps with a partially identified muon (passing all the muon identification except calorimeter energy cut) (Figure 4.9).

Finally, we have developed energy dependant mass cut in tau identification. In the CDF default tau identification, the visible mass (the mass of π^0 and tracks) is

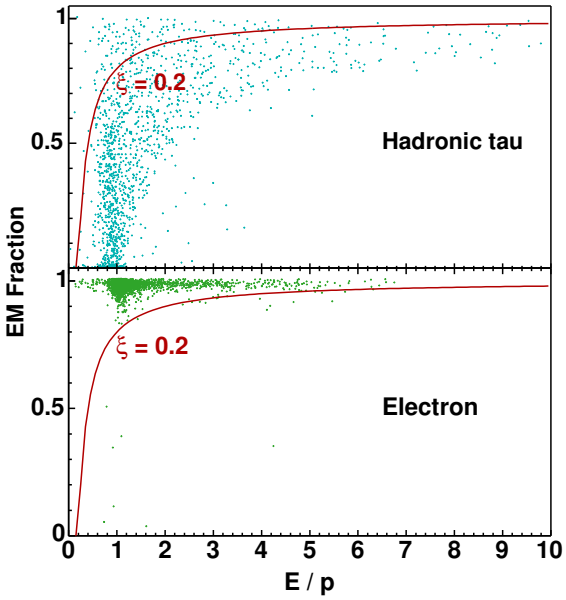

Figure 4.6: **ξ-based electron removal in tau identification.** The EM fraction $\frac{E_{EM}}{E_{total}}$ is the ratio of electromagnetic energy to total energy. ξ-based selection removes electrons having a large EM fraction, but also removes some taus with large EM fraction.

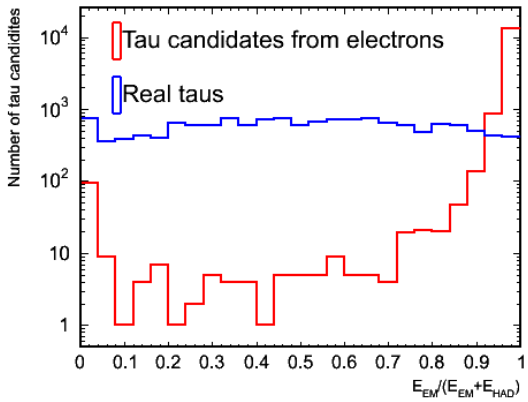

Figure 4.7: **The EM Fraction Distributions from Electrons and Taus.** Some taus also have large EM fraction.

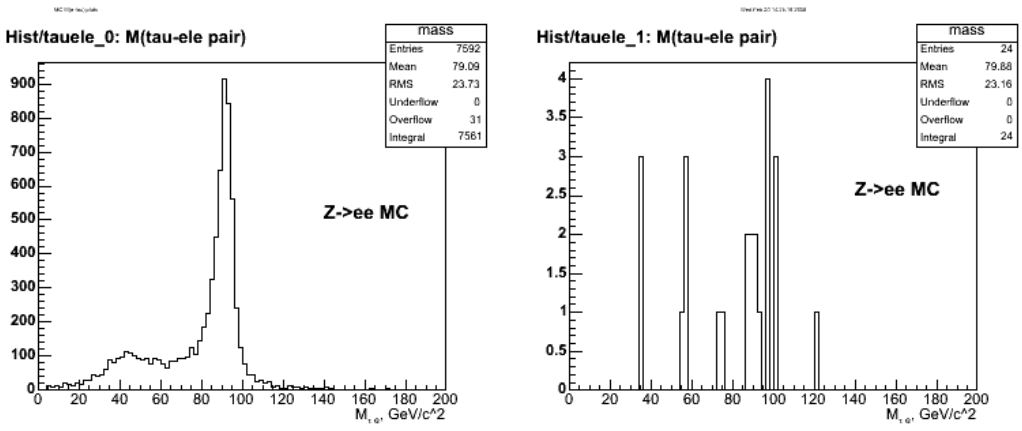

Figure 4.8: **Rejecting Electrons from Tau Candidates.** The invariant mass of an electron and a tau candidate reconstructed in $Z \rightarrow ee$ decays (Monte Carlo generated sample). The left plot shows the tau candidates before the electron removal cut is applied. The right plot shows the tau candidates after the electron removal cut is applied, where Z peak made by the misidentified taus is significantly reduced. By applying an electron removal cut, we have rejected most misidentified tau candidates coming from the electrons.

required to be less than 1.8 GeV/c^2. The calorimeter mass (the mass of the four-momentum which is determined by the energy and position of the calorimeter tower) is required to be less than 4 GeV/c^2. We found that for high energy taus (from high-mass $\tilde{\nu}_\tau$ decay), the fixed mass cut becomes inefficient because the mass distributions become wider than the cut values (Figure 4.10). Therefore, we apply a "sliding mass cut" which is a function of the tau energy (Figure 4.11). The sliding mass cut was chosen so that the efficiency of the cut is constant at 95% as the energy of the tau increases (Figure 4.12).

Taus identification criteria described above are summarized in Table 4.4.

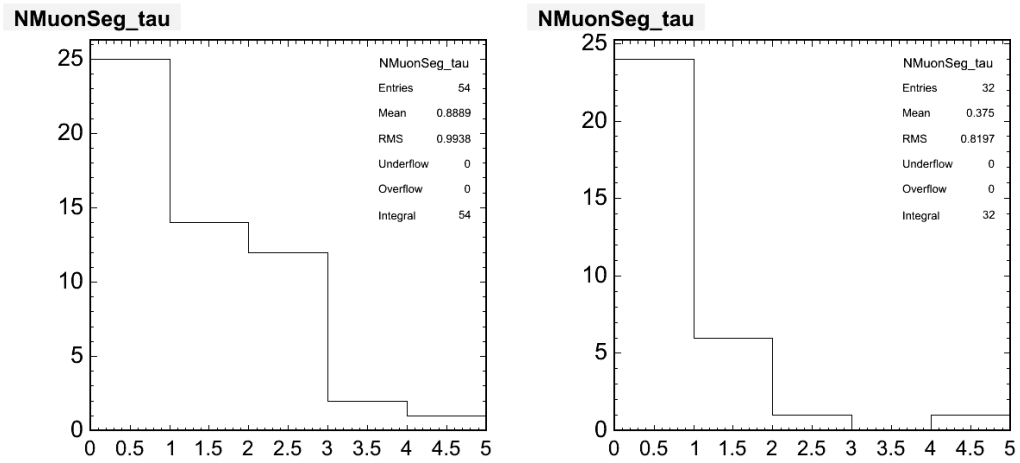

Figure 4.9: **The Number of Muon Stubs Produced by Tau Candidates.** The left plot is the distribution before rejecting muons, where the muons fake tau candidates and produce muon stubs (Monte Carlo generated samples). The right plot is the distribution after rejecting muons, where the fake taus are removed and the most remaining tau candidates don't have the muon stubs (Monte Carlo generated samples).

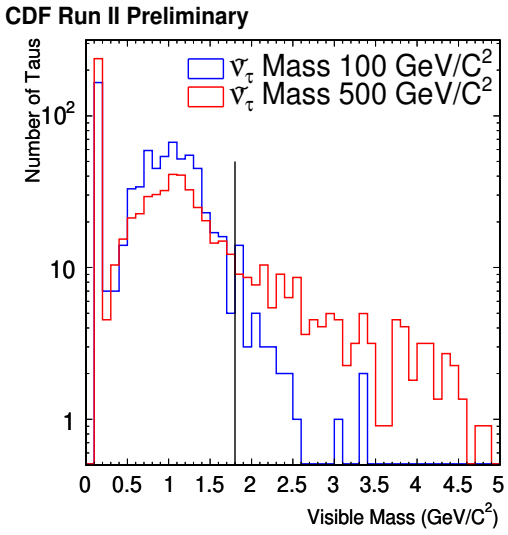

Figure 4.10: **Visible Mass of Taus from Different Mass $\tilde{\nu}_\tau$ Decays.** The visible mass distribution of τ's from 500 GeV/c^2 $\tilde{\nu}_\tau$ decay is broader than the distribution of τ's from 100 GeV/c^2 $\tilde{\nu}_\tau$ decay. The fixed mass cut ($<$ 1.8 GeV/c^2) is not efficient for high-energy taus.

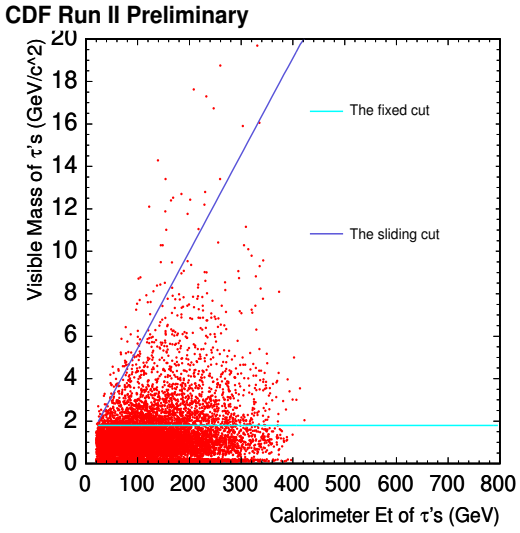

Figure 4.11: **Sliding Tau Visible Mass Cut vs. Fixed Visible Mass Cut.** By apply the sliding visible mass cut, the τ's between the dark blue line (sliding mass cut) and light blue line (fixed mass cut) are recovered.

	CDF Default τ identification	New tau identification
$\|\eta\|$	≤ 1.0	≤ 1.0
Seed Track P_T	≥ 10 GeV/c	≥ 10 GeV/c
Visible E_T	≥ 25 GeV	≥ 25 GeV
Cal E_T	≥ 20 GeV	≥ 20 GeV
Electron removal	ξ based	explicitly
Muon removal	-	yes
Seed tower E_T	≥ 10 GeV	≥ 10 GeV
Seed track $\|Z_0\|$	≤ 60.0 cm	≤ 60.0 cm
Seed track $\|Z_{COT}\|$	≤ 155.0 cm	≤ 155.0 cm
Seed track $\|D_0\|$	≤ 0.2 cm	≤ 0.2 cm
Seed track χ^2_{cot}	≤ 3	≤ 3
Seed track ZCes	9 cm$\leq \leq 230$ cm	9 cm$\leq \leq 230$ cm
1-prong |XCes|	$\leq$21.5 cm	$\leq$21.5 cm
Seed track COT Ax. Seg.	≥ 3 (5)	≥ 3 (5)
COT St. Seg.	≥ 3 (5)	≥ 3 (5)
Number of isolated tracks	0	0
Calorimeter Isolation	≤ 0.1	≤ 0.1
CalMass	$\leq$4.0 GeV/c^2	$\leq 4.0 + (20.0 - 4.0) \times \frac{E_T - 20.0}{400.0 - 20.0}$
TrkMass	$\leq$ 2.0 GeV/c^2	$\leq$ 2.0 GeV/c^2
VisMass	$\leq$ 1.8 GeV/c^2	$\leq 1.8 + (10.0 - 1.8) \times \frac{E_T - 20.0}{200.0 - 20.0}$

Table 4.4: **List of Tau Identification Criteria.**

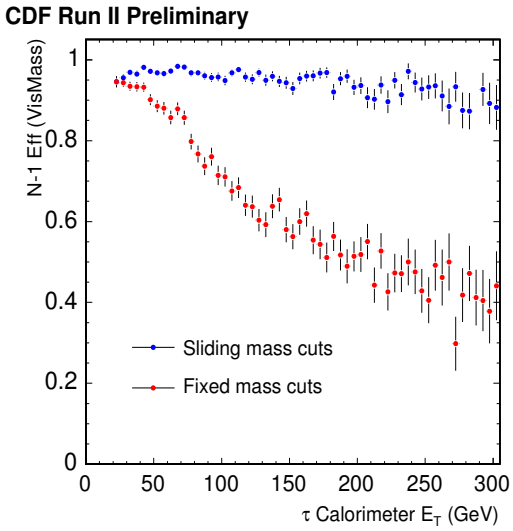

Figure 4.12: **Visible Mass Cut Efficiency.** The efficiency of the sliding visible mass cut is constant when the energy of tau increases (blue), while the efficiency of the fixed cut decreases when the energy of tau increases (red).

4.3.1 Tau Identification Efficiency ϵ_τ and Scale Factor

Tau identification efficiency is the probability of a tau candidate passing the identification selection. We measure the tau identification efficiency in data ($\epsilon_\tau^{\rm data}$) and Monte Carlo generated sample ($\epsilon_\tau^{\rm MC}$). The ratio of $\epsilon_\tau^{\rm data}$ and $\epsilon_\tau^{\rm MC}$ is referred to as the scale factor, which can be used to rescale the $\epsilon_\tau^{\rm MC}$.

The tau identification efficiency is calculated as:

$$\epsilon_\tau = \frac{\rm N_T}{\rm N_P} \tag{4.6}$$

where $\rm N_P$ is the number of tau candidates with $|\eta| \leq 1.0$, $\rm P_T \geq 10$ GeV/c and visible $\rm E_T \geq 25$ GeV, and $\rm N_T$ is the number of taus passing all the identification criteria. We use $W \rightarrow \tau\nu$ events to measure the $\epsilon_{\tau \rm ID}$. The scale factor between data and Monte Carlo generated sample is $\epsilon_\tau^{\rm data}/\epsilon_\tau^{\rm MC} \simeq 1$ [13].

4.3.2 Jet-to-Tau Misidentification Probability

It is difficult to identify hadronic taus in a hadron collider environment. Some narrow QCD jets consisting π^0, $\pi^{\pm}$ and $K^{\pm}$ can appear similar to tau decays. The tau identification criteria, for instance the isolation and the mass criteria, are designed to remove the QCD background. However, some tau candidates reconstructed from QCD jets can pass the tau identification.

To study the probability for those tau-like candidates from jets to be misidentified as taus, we use the following triggered data samples: Jet20, Jet50, Jet70, Jet100; and Monte Carlo generated samples Jet300 (Jet500). The jet-to-tau misidentification probability is defined as:

$$\mathrm{P}^{\tau}_{\mathrm{mis}} = \frac{\mathrm{N}_{\mathrm{tight}}}{\mathrm{N}_{\mathrm{candidates}}} \tag{4.7}$$

where $\mathrm{N}_{\mathrm{candidates}}$ is the number of tau candidates with calorimeter $\mathrm{E_T} > 20$ GeV in Jet20 sample (> 50 GeV in Jet50 sample, etc.), seed track $\mathrm{P_T} > 10$ GeV/c, seed track (9 cm $< |\mathrm{Z_{CES}}| <$ 230 cm) in the jet samples, and $\mathrm{N}_{\mathrm{tight}}$ is the number of denominator candidates passing the tight tau identification selection.

We measure $\mathrm{P}^{\tau}_{\mathrm{mis}}$ in QCD data samples as a function of the tau calorimeter energy. However, because the QCD dijet cross section decreases rapidly when jet energy increases, we don't have enough statistics in the high energy region in data sample (especially above 200 GeV). We have to use Monte Carlo samples to estimate the jet-to-tau misidentification probability in the high energy region. We found that some tau variables are not simulated well because Monte Carlo simulated tau jets are more narrow than the tau jets in data [14]. We tuned the tau variables in the Monte Carlo samples by using the procedures described in [14]. As a result, the jet-to-tau misidentification probabilities determined by using the tuned Monte Carlo are consistent with the misidentification probabilities measured in data (the ratio of them is $S = 0.95 \pm 0.16$). We also found that $\mathrm{P}^{\tau}_{\mathrm{mis}}$ in different jet samples are consistent within the statistical uncertainty.

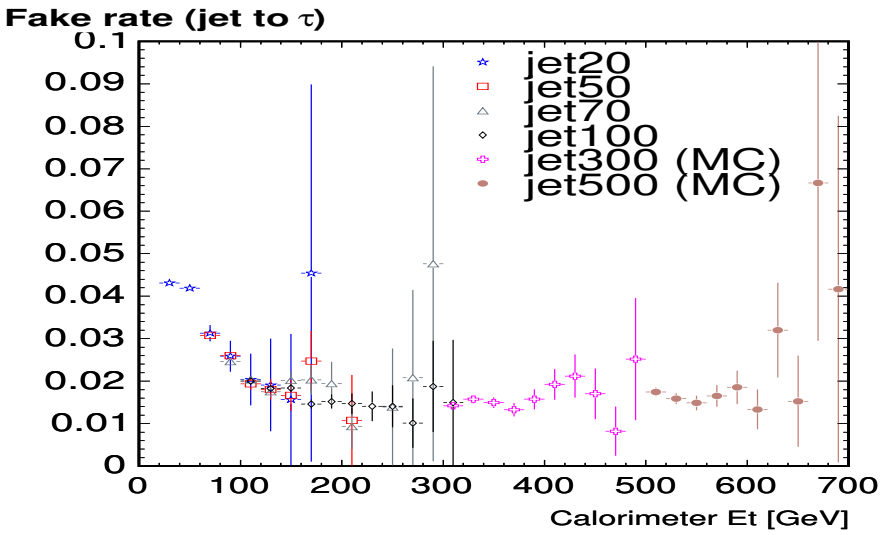

Figure 4.13: **Jet-to-Tau Misidentification Probability.** We found that the misidentification probability in different samples are consistent within the statistical uncertainty. The misidentification probability in the Monte Carlo generated samples are consistent with the extrapolation from the data.

Figure 4.13 shows the P^{τ}_{mis} measured in data samples and the Monte Carlo samples.

4.3.3 Electron-to-Tau Misidentification Probability

To measure the probability of an electron being misidentified as a tau, we use electrons from Z boson decay. We identify $Z \rightarrow ee$ decays by requiring one of the electrons to be a "loose electron" (passing the identification criteria listed in Table 4.3). The second electron, as the probe, is required to be reconstructed by the tau reconstruction algorithm. The dilepton mass is in the region 80 GeV $< M_{e\tau} <$ 100 GeV.

The electron-to-tau misidentification probability is defined to be:

$$P^{e-\tau}_{mis} = \frac{N}{N_0} \tag{4.8}$$

where N_0 is the number of Z events reconstructed from a loose electron and a

tau candidate passing the tau identification criteria except for electron removal and N is the subset of denominator events, which have the tau candidates pass all the tau identification criteria including the electron removal. We do the measurement in data and the Monte Carlo sample. The measured electron-to-tau misidentification probabilities are $P_{data} = (1.6 \pm 0.9)$ % and $P_{MC} = (2.0 \pm 0.4)$ % [15].

Chapter 5

Search

5.1 Data and Monte Carlo Samples

5.1.1 Data Samples

We use Run II data in the run range 150145–212133 collected over the period 02/2002-02/2006. The runs with sub-detectors functioning properly for lepton reconstruction are selected. The data are triggered by the high$-\mathrm{P_T}$ lepton trigger paths: ELECTRON_CENTRAL_18, MUON_CMUP_18, MUON_CMX_18 (Table 5.1). The integrated luminosity is 1 pb^{-1}.

5.1.2 Signal and Background Monte Carlo Samples

We generate the Higgs boson H, a scalar resonance available from the PYTHIA generator, and produce d quark and anti-d quark $d\bar{d} \rightarrow H$ event samples. The PYTHIA event generator with the CTEQ5L parton distribution function (PDF) and the CDF run II detector simulation based on GEANT 3 are used to generate the simulated samples. We force the scalar to decay into different flavor leptons $e\mu,\ e\tau,\ \mu\tau$; the Next-to-Leading order (NLO) $\widetilde{\nu}_\tau$ theoretical cross section is used for the absolute normalization. The scalar is generated at nine mass points from

Trigger Level	CEM18	CMUP18	CMX18
Level 1	$E_T \geq 8$ GeV XFT_$P_T \geq 8$ GeV/c $E_{HAD}/E_{EM} \leq 0.125$	$P_T \geq 6$ GeV/c XFT_$P_T \geq 4.1$ GeV/c CMP Stub	$E_T \geq 6$ GeV/c XFT_$P_T \geq 8.3$ GeV/c
Level 2	$E_T \geq 16$ GeV XFT_$P_T \geq 8$ GeV/c $E_{HAD}/E_{EM} \leq 0.125$	XFT_$P_T \geq 8.3$ GeV/c CMU stub CMP stub	XFT_$P_T \geq 10.1$ GeV/c CMX stub
Level 3	$E_T \geq 18$ GeV XFT_$P_T \geq 9$ GeV/c $E_{HAD}/E_{EM} \leq 0.125$ Lshr ≤ 0.4 $\Delta Z_{CEM} \leq 8$ cm	$P_T \geq 18$ GeV/c $\Delta X_{CMU} \leq 20$ cm $\Delta X_{CMP} \leq 20$ cm	$P_T \geq 18$ GeV/c $\Delta X_{CMX} \leq 10$ cm

Table 5.1: **High$-P_T$ Lepton Trigger Requirements.**
ELECTRON_CENTRAL_18, MUON_CMUP_18 and MUON_CMX_18 trigger paths require events that meet the listed criteria.

Lepton type	scale factor	trigger efficiency
CEM	0.98	0.96
CMUP	0.87	0.91
CMX	0.99	0.97
TAU	1.0	–

Table 5.2: **Lepton identification Scale Factors and Trigger Efficiencies.**

50 GeV/c^2 to 800 GeV/c^2. We use the Electroweak Group Monte Carlo samples for modelling the SM processes.

We emulate the trigger effect on the Monte Carlo samples by weighting the event yields with the trigger efficiency. The scale factors of lepton identification efficiencies are also applied to the event yields in Monte Carlo samples, where the scale factor is the ratios of the identification efficiency measured in data and the Monte Carlo sample. Table 5.2 lists the scale factors and trigger efficiencies used in the analysis [16] [17].

5.2 Event Level Selection

We select two leptons of different flavor and opposite electric charge. The two leptons have to pass the lepton identification criteria described above. We require that the distance between the two leptons in the z-coordinate ΔZ < 5 cm and the distance in $\eta - \phi$ plane ΔR > 0.4.

If there are three identified leptons in the event, two of which are of same flavor, we select the most energetic one among these. If the three leptons have different flavor, the event simultaneously belongs to all three search channels.

5.3 Signal Acceptance

The CDF detector only accepts some of the events produced in collisions due to the geometrical limitations of the subdetectors. In addition, the efficiencies of reconstruction and identification are not 100%. Therefore, the number of expected events is as follows:

$$N_{exp} = (\sigma \times BR) \times \mathcal{L}_{int} \times \alpha_{total} \tag{5.1}$$

where N_{exp} is number of the expected events, and α_{total} is the probability of the events being detected, reconstructed and identified. We use the Monte Carlo generated sample to measure α_{total}, where we know how many physical events are produced at generator level. The α_{total} is defined as the number of the events passing all event selection divided by the number of generated events. We scale α_{total} from Monte Carlo to data by applying the trigger efficiencies and lepton identification scale factors.

We apply the identification cuts described in chapter 4 to leptons in signal Monte Carlo samples. Compared to the standard electron identification algorithm, the new electron identification efficiency has been improved by $\sim 10\%$ (Figure 5.1). We also have improved the tau identification efficiency by factor of two by using the new tau identification algorithm (Figure 5.1).

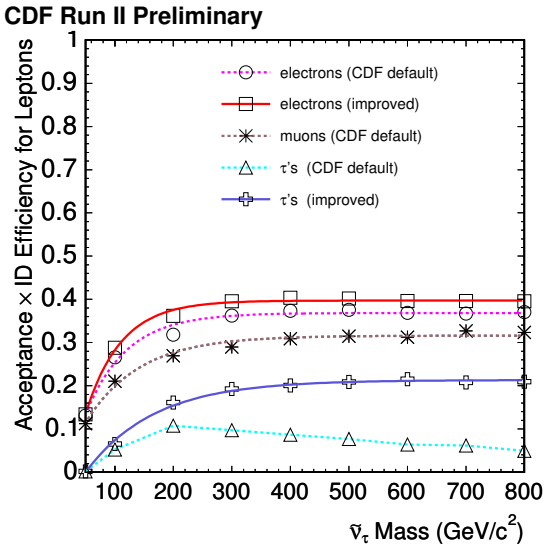

Figure 5.1: **Improved Lepton Acceptances.** The tau identification efficiency decreases when the energy of tau increases if we use CDF default identification criteria (light blue). The tau identification efficiency stays constant in the high energy region by using the new criteria (dark blue). In addition, the tau identification efficiency has been improved by factor of two by using the new criteria. The electron identification efficiency has been improved by $\sim 10\%$ by using the new criteria.

The acceptances for signal events using the new identification criteria in their channels are shown in Figure 5.2.

5.4 Standard Model Backgrounds

5.4.1 Physics Backgrounds

"Physics" backgrounds are those SM processes having the same signature as the signal. In our analysis, the following processes contribute as the physics backgrounds:

Drell-Yan production: Drell-Yan processes are the annihilation of a quark anti-quark pair to produce a Z boson or virtual photon which decays into a lepton

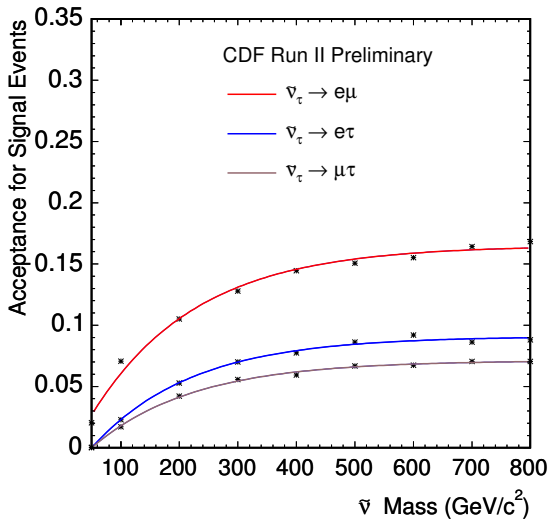

Figure 5.2: **Signal Event Acceptances.** The lots show the acceptances of $\tilde{\nu}_\tau \to e\mu, e\tau, \mu\tau$. The acceptances in e$\tau$ and $\mu\tau$ channels are lower than the on in the eμ channels because we only select hadronic tau decays and the tau identification efficiency is lower than electron or muon.

pair ($p\bar{p} \to Z/\gamma^* \to \ell^+\ell^-$). When Z/γ^* decays into $\tau\tau$, where one τ decays leptonically into e or μ and another τ decays hadronically, Drell-Yan becomes a background in the $e\tau$ or $\mu\tau$ channel. When both τ's from Z/γ^* decay leptonically, Drell-Yan becomes a background in the $e\mu$ channel. The PYTHIA generated Monte Carlo sample correctly models the theoretical $\sigma \times Br$ of $Z/\gamma^* \to \ell^+\ell^-$, which is 485 pb at Next-to-Leading order (NLO) if the mass is larger than 20 GeV/c^2 [18].

Diboson production: diboson production refers to the interactions between gauge bosons. The diboson production cross section is much smaller than the Drell-Yan process. The NLO theory production cross section is 12.4 pb for WW, 3.7 pb for WZ and 1.4 pb for ZZ [19]. When both gauge bosons decay into leptons of different flavors, the diboson production becomes a physics background in this analysis.

Top quark pair production top quark pairs are produced through the strong interactions ($p\bar{p} \to t\bar{t}$ or $gg \to t\bar{t}$). Top quarks decay into Wb with a branching ratio of almost 100%. If the two W bosons from top quark decay into leptons of different flavor, the top pair production becomes a physics background in this analysis. The NLO theoretical top pair production cross section is 6.7 pb for a top quark with mass of 175 GeV/c^2[20].

To estimate the contributions from the physics backgrounds, we apply the event selection to the Monte Carlo generated samples. The NLO theoretical cross section is used for the absolute normalization. The predicted background is the number of events passing selection from the Monte Carlo sample normalized to the same integrated luminosity as data and scaled by the trigger efficiency and lepton identification scale factor.

5.4.2 Fake Backgrounds

There are also backgrounds due to lepton misidentification. We call them "fake backgrounds". If one lepton in an event is a misidentified object, we call the event a "single fake" event. If both leptons are misidentified objects, we call the event a "double fake" event.

The single fake backgrounds in this analysis include:

W+jet(s): one or more jets can be produced by QCD interactions associated with a W boson in an event. The measured cross section of inclusive production times branching ratio of $W \to \ell\nu$ is 2775 pb at CDF[22]. W+jet(s) production becomes a background in our analysis when W bosons decay leptonically into e/μ/τ and a jet is misidentified as a lepton.

Drell-Yan+jet(s): one of the leptons from Z/γ^* decays is missing. A jet is misidentified as a lepton.

Drell-Yan ($p\bar{p} \to Z/\gamma^* \to ee$): one electron is misidentified as a tau.

Drell-Yan ($p\bar{p} \rightarrow Z/\gamma^* \rightarrow \mu\mu$): one muon is misidentified as an election or tau.

We use the Monte Carlo samples to estimate the single fake backgrounds.

The double fake backgrounds include:

QCD dijets: the two jets are misidentified as leptons.

γ + jets: the γ is misidentified as an election and a jet is misidentified as a τ or μ.

To estimate double fake backgrounds, we use events with same charge leptons in data since there is no correlation between the charge of the leptons in dijet and γ+jet events. We need to subtract the contribution of the same charge events originating from backgrounds other than QCD dijets and γ + jets.

5.5 "Blind" Analysis

The analysis is performed as a counting experiment in which the number of observed events in data will be compared with the number of predicted events from SM background. Meanwhile, to eliminate the experimenter's bias on the results, we perform the analysis as a "blind" analysis. Control regions and signal regions are defined, which will be described in the following discussions. Before we apply the event selection to data in signal regions, we validate the event selection and the background predictions in the control regions by checking the consistency between the expectation from SM background and the event yields in data.

5.5.1 Control Regions

The control region is defined as: 50 GeV/c^2 $< M_{LL} <$ 110 GeV/c^2, where M_{LL} is the dilepton mass. We use the tau visible four-momentum (introduced in chapter 4) plus electron or muon four-momentum to reconstruct the dilepton mass in $e\tau$ and $\mu\tau$ channels. To estimate the amount of expected SM background, we apply the

event selection to the tuned PYTHIA Monte Carlo samples. The number of events selected in Monte Carlo samples are scaled by the lepton identification scale factors and trigger efficiencies which are listed in Table 5.2. In the control regions, the dilepton mass distributions from the SM predicted backgrounds and the observation in data in three channels are shown in Figure 5.3. The dominant backgrounds are: Drell-Yan ($\tau\tau$) and the fake backgrounds in the $e\tau$ and $\mu\tau$ channels; Drell-Yan ($\tau\tau$), WW and $t\bar{t}$ in the $e\mu$ channel (the contribution from the fake backgrounds are much smaller than the physics backgrounds). This is understandable because the misidentification probability for taus is higher than misidentification probability for an electron or muon.

In addition to the dilepton mass distributions, we also compare other variable distributions from the SM predicted backgrounds and the observation in data in the control regions. The distributions are selected because they are powerful discriminants between different backgrounds or they indicate how well the Monte Carlo simulates data. For instance:

The tau visible mass distribution is shown in Figure 5.4, where the visible mass of most misidentified taus from jets is larger than real taus from physics background.

The tau track multiplicity distribution is shown in Figure 5.5, where we select the 1-prong and 3-prong taus. The ratio of the 1-prong and 3-prong taus is approximately $3 : 1$. However, since the reconstruction efficiencies for 1-prong and 3-prong are different (the probability for π^0s to carry a significant amount of the tau energy is larger for 1-prong taus than 3-prong taus. While it is easier to reconstruct tracks than π^0s.), the ratio of the identified 1-prong and 3-prong taus is not exactly $3 : 1$. The fake taus from jets tend to have more tracks than real taus.

The tau visible energy distribution is shown in Figure 5.6, where the tau visible energy is less than the real energy of the tau because the neutrino from tau decays escapes detection.

The tau isolation energy in hadronic calorimeter and electromagnetic calorimeter

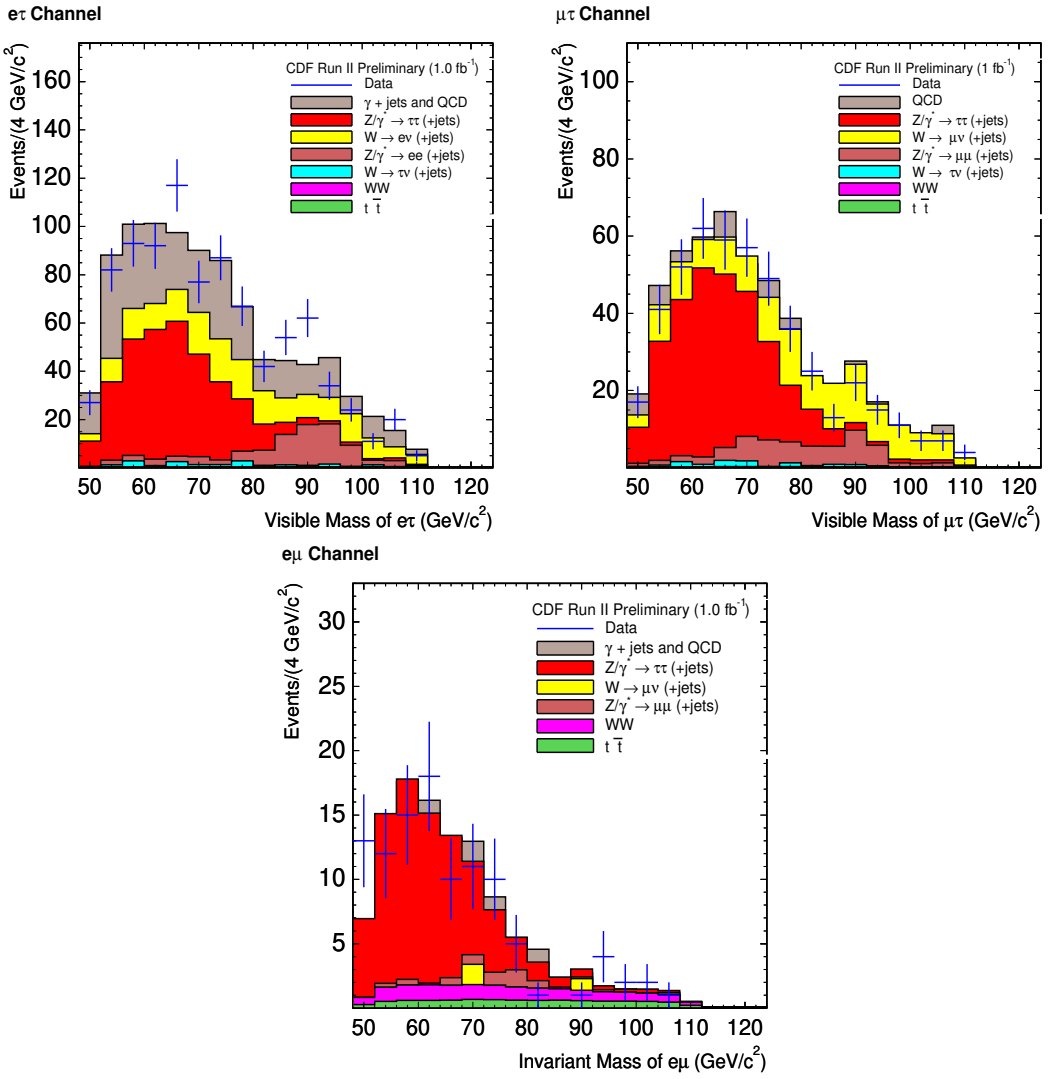

Figure 5.3: **Dilepton Mass Distributions in the Control Regions.** We use the visible four-momentum of the tau plus the electron or muon four-momentum to reconstruct dilepton masses in $e\tau$ and $\mu\tau$ channels. The dominant backgrounds are: Drell-Yan ($\tau\tau$) and the fake backgrounds in the $e\tau$ and $\mu\tau$ channels; Drell-Yan ($\tau\tau$), WW and $t\bar{t}$ in the $e\mu$ channel (the contribution from the fake backgrounds is much smaller than the physics backgrounds).

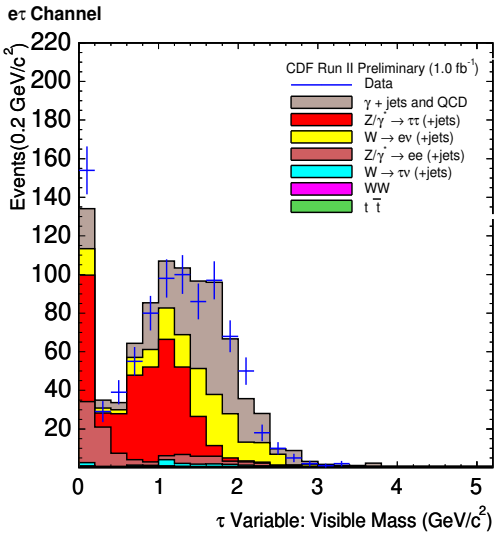

Figure 5.4: **Tau Visible Mass Distribution in the $e\tau$ Channel Control Region.** The visible mass of most misidentified taus from jets (grey and yellow colors) is larger than real taus from physics background.

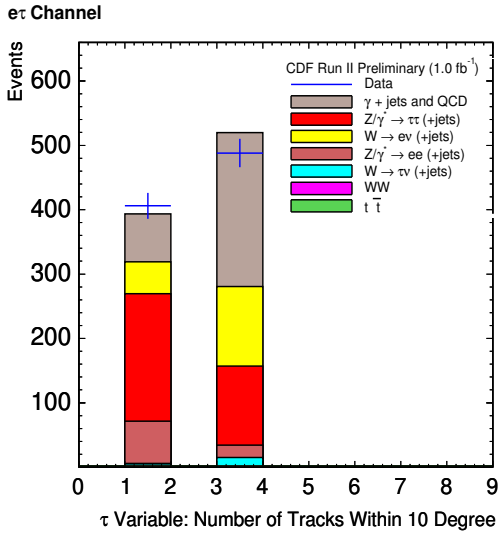

Figure 5.5: **Tau Track Multiplicity Distribution in the $e\tau$ Channel Control Region.**

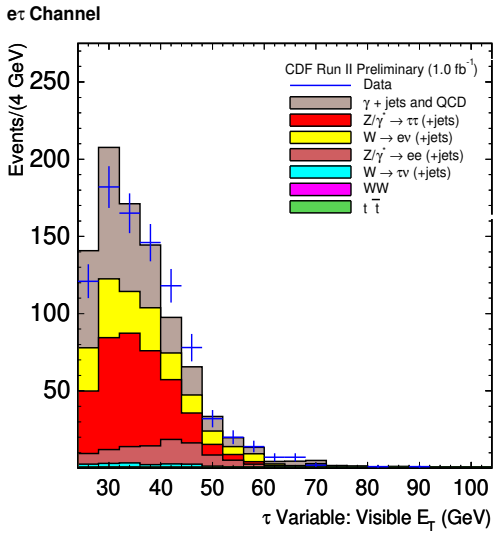

Figure 5.6: **Tau Visible Energy Distribution in the $e\tau$ Channel Control Region.** The tau visible energy is less than the real energy of the tau because the neutrino from the tau decay escapes the detection.

distributions are shown in Figure 5.7 and Appendix Figure A.1, where the isolation energy is the energy measured around the tau within the cone $R \leq 0.4$ in the calorimeters (except for the tau energy). The isolation energy is not simulated well in the Monte Carlo generated samples and is tuned using data.

The electron isolation energy E_{iso} over the total energy is shown in Figure 5.8, where the misidentified electrons from jets have a larger E_{iso}/E than the real electrons.

More figures showing other distributions that we compared between the predicted SM backgrounds and the observations in data are in the Appendix.

As a conclusion for this section, the number of observed events and expected events from the SM background in the control region agree well, as summarized in Table 5.3.

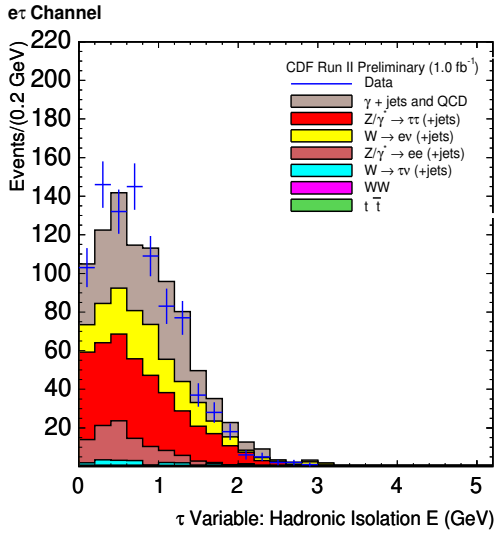

Figure 5.7: **Tau Hadronic Isolation Energy in the $e\tau$ Channel Control Region.** The isolation energy is not simulated well in the Monte Carlo generated samples and is tuned to match data.

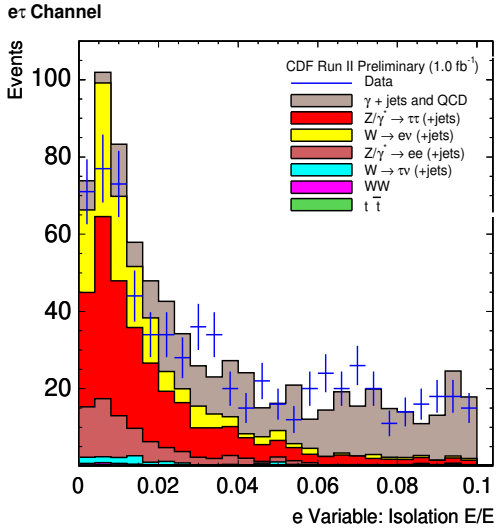

Figure 5.8: **Electron Isolation Energy over the Total Energy in the $e\tau$ Channel Control Region.** The misidentified electrons from jets have a larger E_{iso}/E than the real electrons.

SM processes	eτ channel	eμ channel	$\mu\tau$ channel
$Z/\gamma^* \to \tau\tau$	321.0 ± 4.2	77.6 ± 2.1	272.2 ± 4.0
$Z/\gamma^* \to ee$	84.7 ± 3.7	–	–
$Z/\gamma^* \to \mu\mu$	–	5.8±1.0	54.5 ± 3.0
$W \to e\nu$(+jets)	173.0 ± 9.4	–	–
$W \to \mu\nu$(+jets)	–	2.5±1.5	144.3 ± 11.8
$W \to \tau\nu$(+jets)	16.1 ± 2.2	–	8.7 ± 1.7
WW	2.7 ± 0.05	14.0± 0.1	2.3 ± 0.04
$t\bar{t}$	2.1 ± 0.04	8.6±0.1	1.7 ± 0.04
Dijets and γ +jets	313.8 ± 20.5	1.1±2.7	22.0 ± 11.8
Total predicted background	913.4 ± 23.3 ± 47.0	109.5 ±3.9± 7.5	505.7 ±17.5± 38.8
Observation	894	105	477

Table 5.3: **The Predicted Backgrounds and Observation in the Control Regions.** The uncertainties on the individual backgrounds are statistical and on the total predicted background are statistical and systematic.

5.5.2 Signal Regions

We have defined eight signal regions in each channel assuming that the mass of $\widetilde{\nu}_\tau$ is between 100 GeV/c^2 and 800 GeV/c^2. For a given $\widetilde{\nu}_\tau$ mass, the corresponding signal region is defined as $M_{LL} > M_{LL}^{min}$, where M_{LL} is the dilepton mass from $\widetilde{\nu}_\tau$ decays and M_{LL}^{min} is the lower bound of the signal region. The number of signal events and the background events in a given signal region are obtained by integrating their dilepton mass distribution from M_{LL}^{min} to the infinity ($\sim$ 1 TeV). M_{LL}^{min} is chosen such that we can obtain the best expected limit on $\sigma \times$ BR of $\widetilde{\nu}_\tau$ for a given $\widetilde{\nu}_\tau$ mass in a given channel. For this purpose, we are "blind" to the real number of events observed in data(N_{data}^{obs}) in an "a priori" signal region. Instead, we assume that the number of observed events (N_{data}^{obs}) is derived from the fluctuation of the number of expected SM background events (N_{bg}^{exp}) in that region, and simulate pseudo-experiments. Then we translate N_{data}^{obs}, N_{bg}^{exp}, and the signal acceptance into the expected upper limit on the $\sigma \times BR$ of $\widetilde{\nu}_\tau$ using a Bayesian technique [21]. Driven by obtaining the

signal mass (GeV/c^2)	M_{LL}^{min} in $e\tau$ channel (GeV/c^2)	M_{LL}^{min} in $\mu\tau$ channel (GeV/c^2)	M_{LL}^{min} in $e\mu$ channel (GeV/c^2)
100	80	80	90
200	160	160	190
300	230	220	280
400	280	240	360
500	310	280	450
600	340	320	500
700	360	350	550
800	360	370	600

Table 5.4: **Signal Regions.** Table shows the lower bound M_{LL}^{min} of each signal region corresponding to the different $\widetilde{\nu}_\tau$ masses in three channels.

best expected limit, for $\widetilde{\nu}_\tau$ with mass 500 GeV/c^2, the signal region is defined as $M_{LL}^{min} = 310$ GeV/c^2 in the $e\tau$ channel, $M_{LL}^{min} = 280$ GeV/c^2 in the $\mu\tau$ channel. For $\widetilde{\nu}_\tau$ with mass 600 GeV/c^2, the signal region is defined as $M_{LL}^{min} > 500$ GeV/c^2 in the $e\mu$ channel (Figure 5.9). The definition of signal regions corresponding to more $\widetilde{\nu}_\tau$ masses are listed in Table 5.4.

Because we have low statistics in the region above 200 GeV/c^2, the backgrounds are estimated by fitting the shape.

Figure 5.10 shows the dilepton mass distribution from the single fake background, $W \to \mu\nu$+jets, where a jet is misidentified as a tau. The solid histogram shows the background events with one tight muon and one tight tau (we have very few events above 200 GeV/c^2). We loosen the identification criteria on tau (only apply the geometric and kinematic cuts) to obtain a more reliable background shape (having more events in high energy region), shown as data points. Then we fit the data points and the fitted shape is shown as the colored line. The black line is the same as the colored line but with the proper normalization. The number of background events in a given mass region is an integration of the fitted shape with the proper normalization.

Figure 5.11 shows the dilepton mass distribution from the physics background

Luminosity	6%
Tau identification efficiency	5%
Jet-to-tau misidentification probability	15 %
Electron identification efficiency	1 %
Muon identification efficiency	1 %
PDF's	see Table 5.6
Background fitting	mass dependant

Table 5.5: **Summary of the Systematic Uncertainties.** The Table lists the various sources of systematic uncertainty in our measurement.

Drell-Yan ($\tau\tau$), where one tau decays into muon. The solid histogram shows the background events with one tight muon and one tight tau. The data points shows the background events with one tight muon and one tight tau before normalization. We fit the data points and the fitted shape is shown as the colored line. The black line is the same as the colored line but with the proper normalization. The number of background events in a given mass region is obtained by integrating the fitted shape with the proper normalization.

5.6 Systematic Uncertainties

There are several sources of systematic uncertainties summarized in Table 5.5. The dominant systematic uncertainties are from the jet-to-tau misidentification probability and the luminosity measurement.

5.6.1 Luminosity

At CDF, the luminosity is determined by using the Cherenkov Luminosity Counters (CLC) and the measurement of the inelastic $p\overline{p}$ scattering cross section. The combined uncertainty from the CLC efficiency and inelastic $p\overline{p}$ scattering cross section is 6%[23], which contribute to the expected signal and background estimate from the

Monte Carlo samples.

5.6.2 Lepton Identification

We use the Monte Carlo samples to estimate the signal and background acceptances, which are scaled by lepton identification scale factors to data. The uncertainties on lepton identification scale factors affect the estimate of the signal acceptance and the predictions on the SM background. The uncertainty on the tau identification efficiency is 5% due to jet contamination in the tau samples and the statistical limitation of samples used for the measurement. The uncertainty on the estimate of jet to tau misidentification probability is 15% [14], which is from the different misidentification probabilities measured in the several jet samples. The uncertainty on the electron identification efficiency and on the muon identification efficiency are 1% respectively [16], which are smaller than tau identification efficiency. This is understandable because it is easier to obtain pure electron/muon samples than pure tau samples.

5.6.3 Background Fitting

We use the fitting method which is described in section 5.5.2 to estimate the background in the signal regions. The uncertainty from the choice of the fitting function and the fitting parameters is translated into the systematic uncertainty. Correlations among the fitting parameters are taken into account when calculating the uncertainty on a individual background. The total background uncertainty is obtained by combining the individual background uncertainties in quadrature.

signal mass	$\Delta A/A(PDF)(\%)$
100 GeV/c^2	$^{+1.0}_{-0.9}$
300 GeV/c^2	$^{+0.26}_{-0.24}$
500 GeV/c^2	$^{+0.12}_{-0.13}$
800 GeV/c^2	$^{+0.08}_{-0.09}$

Table 5.6: **Systematic Uncertainties Due to the PDF's.** PDF uncertainties on acceptance for different $\widetilde{\nu}_\tau$ masses

5.6.4 Parton Distribution Function

Parton distribution functions (PDF's) are the probability densities for seeing a parton with a certain longitudinal momentum fraction. Uncertainties on the signal acceptance due to using different parton distribution functions are calculated. When modelling the signal production process $d\bar{d} \rightarrow \widetilde{\nu}_\tau$, the acceptance variations result only from variations of d-quark momentum distributions.

For all three channels, uncertainties are $\sim$1% at $M_{\widetilde{\nu_\tau}} = 100$ GeV/c^2 and they are reduced to $\sim$0.1% at $M_{\widetilde{\nu_\tau}} > 500$ GeV/c^2 . The mass dependent PDF uncertainties are shown in Table 5.6.

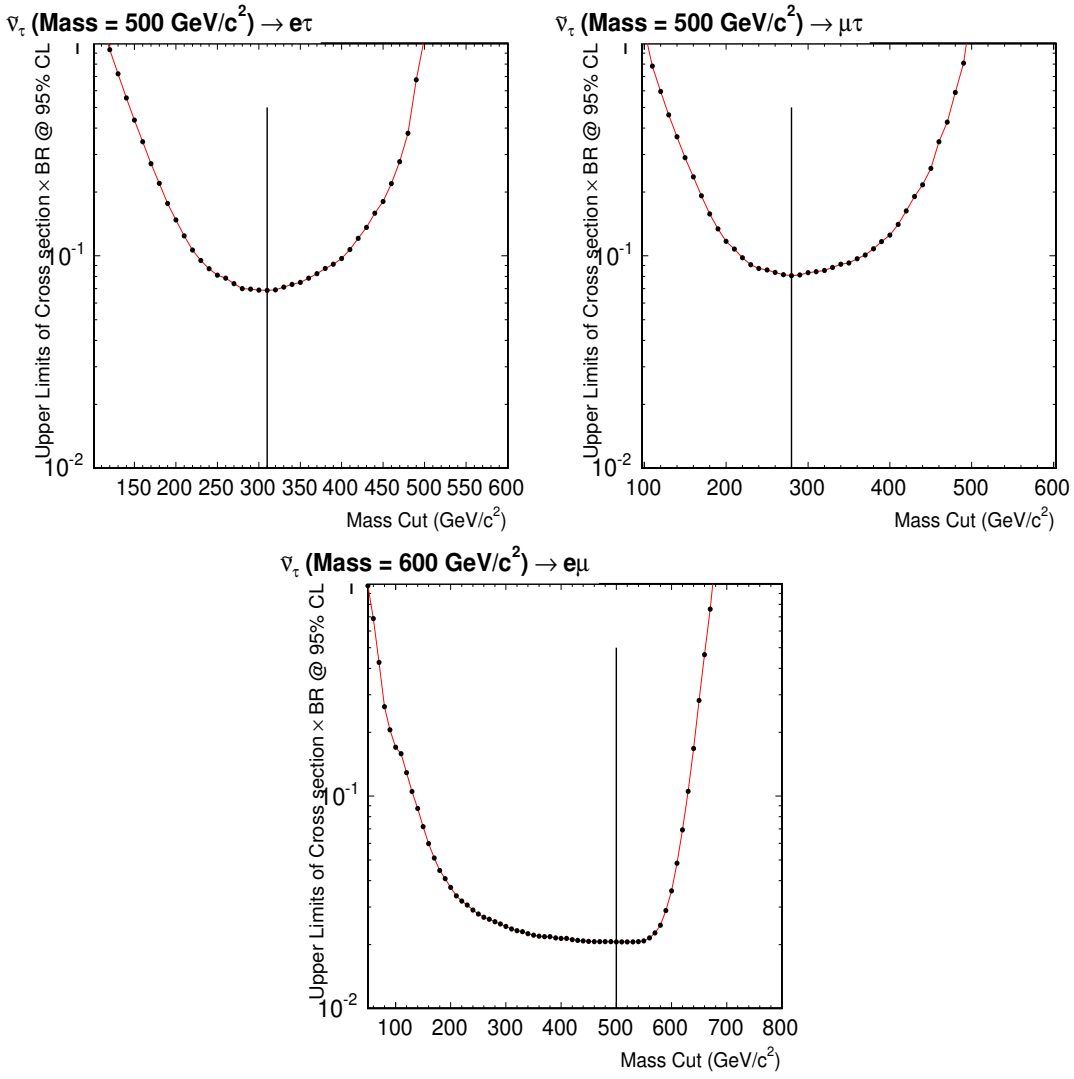

Figure 5.9: **Selecting Lower Bound for Signal Regions.** The plots show the expected upper limits on $\sigma \times \mathrm{BR}$ ($\tilde{\nu}_\tau \rightarrow \mathrm{e}\tau/\mu\tau/\mathrm{e}\mu$) at 95 % C.L. as a function of the lower bound of the signal region. Each point corresponds to the limit derived from the signal acceptance and the integrated background above the corresponding mass selection. The lower bound M_{LL}^{min} is selected at the minimal limit point.

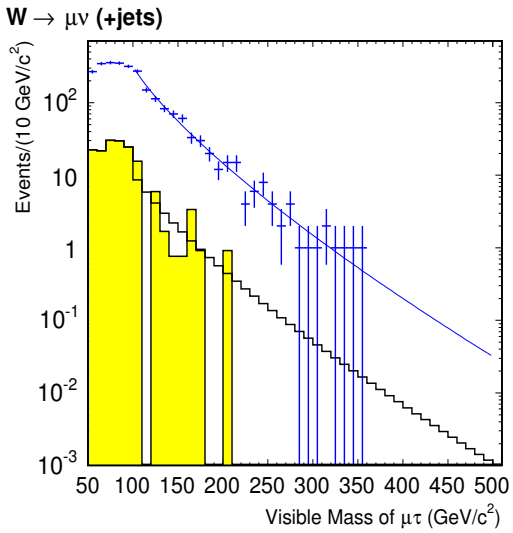

Figure 5.10: **Fitting the Fake Background.** The plot shows the dilepton mass distribution from the single fake background, $W(\mu\nu)$+jets, where jet is misidentified as a tau. The solid histogram shows the background events with one tight muon and one tight tau (we have very few events above 200 GeV/c^2). We loosen the identification criteria on tau (only apply the geometric and kinematic cuts) to obtain a more reliable background shape, shown as data points. Then we fit the data points and the fitted shape is shown as the colored line. The black line is the same as the colored line but after normalization.

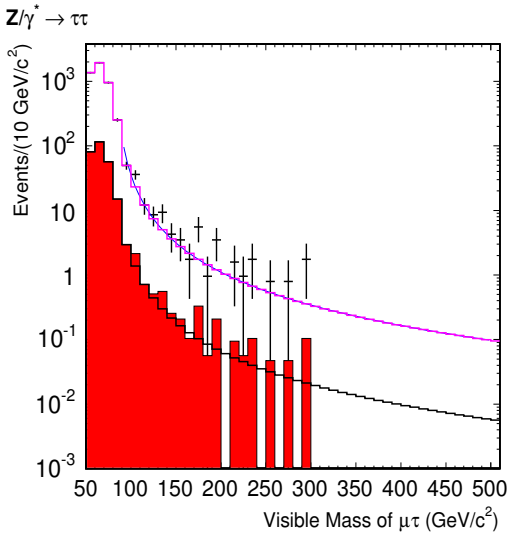

Figure 5.11: **Fitting the Physics Background.** The plot shows the dilepton mass distribution from the physics background, Drell-Yan ($\tau\tau$), where one tau decays into muon. The solid histogram shows the background events with one tight muon and one tight tau. The data points shows the background events with one tight muon and one tight tau before normalization. We fit the data points and the fitted shape is shown as the colored line. The black line is the same as the colored line but after normalization.

Chapter 6

Results

6.1 Opening the Signal Box

After validating the event selection and the SM background predictions in the control regions, we apply the selection to data in the signal regions. The dilepton mass distributions from the SM backgrounds and data are shown in Figure 6.1 (the expected signal events are also presented).

For each given signal region, we compare the observed data with the SM prediction. For instance, in the $e\tau$ channel, we predict 1.4 ± 0.3 events from SM background and observe two events in data in the signal region $M_{LL}^{min} = 310$ GeV/c^2. In the $\mu\tau$ channel, we predict 1.0 ± 0.3 events from the SM background and observe one event in data in the signal region $M_{LL}^{min} = 280$ GeV/c^2. In the $e\mu$ channel, we predict 0.1 ± 0.1 events from the SM background and observe zero events in data in the signal region $M = 500$ GeV/c^2. Table 6.1, Table 6.2 and Table 6.3 show the predicted SM background and the observation in one signal region. Comparisons in additional signal regions defined for $\tilde{\nu}_\tau$ with different masses are listed in Table 6.4.

As a conclusion, the number of events observed in data is consistent with the number of events predicted from the SM background. We find no evidence of physics beyond the SM.

6.2 Interpretation of the Results

Since there is no evidence for new physics in this search, we therefore in the RPV MSSM scenario, set a 95 % C.L. upper limit on $\sigma \times$ BR ($\widetilde{\nu}_\tau \rightarrow e\tau/\mu\tau/e\mu$) as a function of $\widetilde{\nu}_\tau$ mass. The limit is calculated with the number of events observed in data, the number of predicted SM background events (with the uncertainty on it) and the signal acceptance times luminosity (with the uncertainty on it) using the Bayesian technique. The idea of the Bayesian technique can be summarized as follows: when we perform a counting experiment, we predict the number background events b with the uncertainty σ_b and we know the product of the signal acceptance and luminosity, ϵ, with the uncertainty σ_ϵ. The observation is n events in data. If we do the experiments many times, n is a Poison distribution with mean $s\epsilon + b$, where s is the cross section of the process. Our goal is to obtain the upper limit on s with a certain confidence level. To do that, we need to know the posterior probability density function $p(s|n)$ for s [21]. The upper limit on s with 95% C.L. is given by

$$\int_0^{s_u} p(s|n)ds = 95\% \tag{6.1}$$

As a result, the 95% C.L. limits on $\sigma \times$ BR ($\widetilde{\nu}_\tau \rightarrow e\tau/\mu\tau/e\mu$) as a function of the $\widetilde{\nu}_\tau$ in Figure 6.2 and Table 6.4. The expected $\widetilde{\nu}_\tau$ signal event yields correspond to the next-to-leading order (NLO) theoretical $\sigma \times$ BR of Ref. [24] with $\lambda'_{311} = 0.10$ and $\lambda_{i3k} = 0.05$ chosen as the benchmark point. The 95 % C.L. lower limits on the $\widetilde{\nu}_\tau$ mass are 476 GeV/c^2 in the $e\tau$ channel, 471 GeV/c^2 in the $\mu\tau$ channel and 555 GeV/c^2 in the $e\mu$ channel. The mass limits correspond to the intersection of the observed limit and the theoretical prediction which is calculated at the benchmark point.

SM processes	eτ channel
	$M_{LL}^{min} = 310$ GeV/c^2
$Z/\gamma^* \to \tau\tau$	0.7 ± 0.3
$Z/\gamma^* \to ee$	0.04 ± 0.01
$W \to e\nu$(+jets)	0.3 ± 0.05
$W \to \tau\nu$(+jets)	0.002 ± 0.001
WW	0.01 ± 0.002
$t\bar{t}$	0.005 ± 0.001
Dijets and γ +jets	0.3 ± 0.06
Total SM background	1.4 ± 0.3 ±0.1
Observed Events in data	2

Table 6.1: **The Predicted Backgrounds and Observation in the Signal Region $M_{LL}^{min} = 310$ GeV/c^2 in eτ channel.** The uncertainties on the individual backgrounds are statistical and on the total predicted background are statistical and systematic.

SM processes	$\mu\tau$ channel
	$M_{LL}^{min} = 280$ GeV/c^2
$Z/\gamma^* \to \tau\tau$	0.4 ± 0.3
$Z/\gamma^* \to \mu\mu$	0.1 ± 0.02
$W \to \mu\nu$(+jets)	0.3 ± 0.08
$W \to \tau\nu$(+jets)	0.004 ± 0.003
WW	0.02 ± 0.004
$t\bar{t}$	0.006 ± 0.0008
Dijets	0.02 ± 0.005
Total SM background	1.0 ± 0.3±0.1
Observed Events in data	1

Table 6.2: **The Predicted Backgrounds and Observation in the Signal Region $M_{LL}^{min} = 280$ GeV/c^2 in $\mu\tau$ channel.** The uncertainties on the individual backgrounds are statistical and on the total predicted background are statistical and systematic.

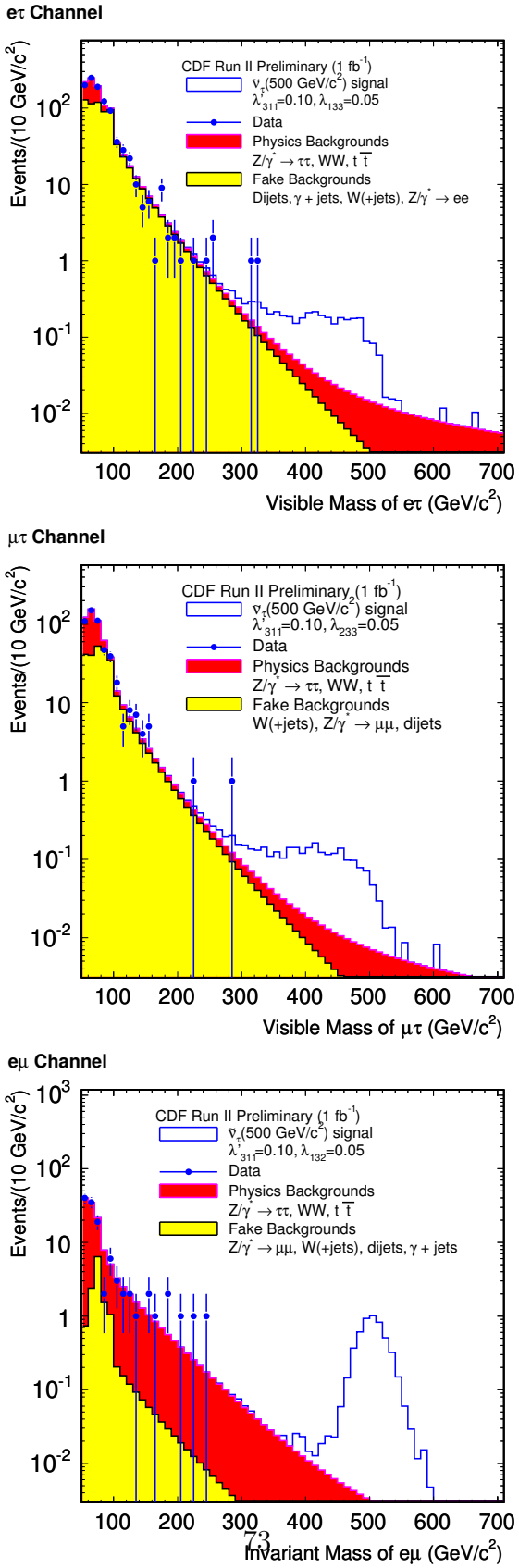

Figure 6.1: **Dilepton Mass Distributions.** The observed data events agree with the SM expectations. The expected signal event yields are calculated using the NLO $\sigma \times$ BR of $\tilde{\nu}_\tau$ ($M_{\tilde{\nu}_\tau} = 500$ GeV/c^2) at the benchmark point.

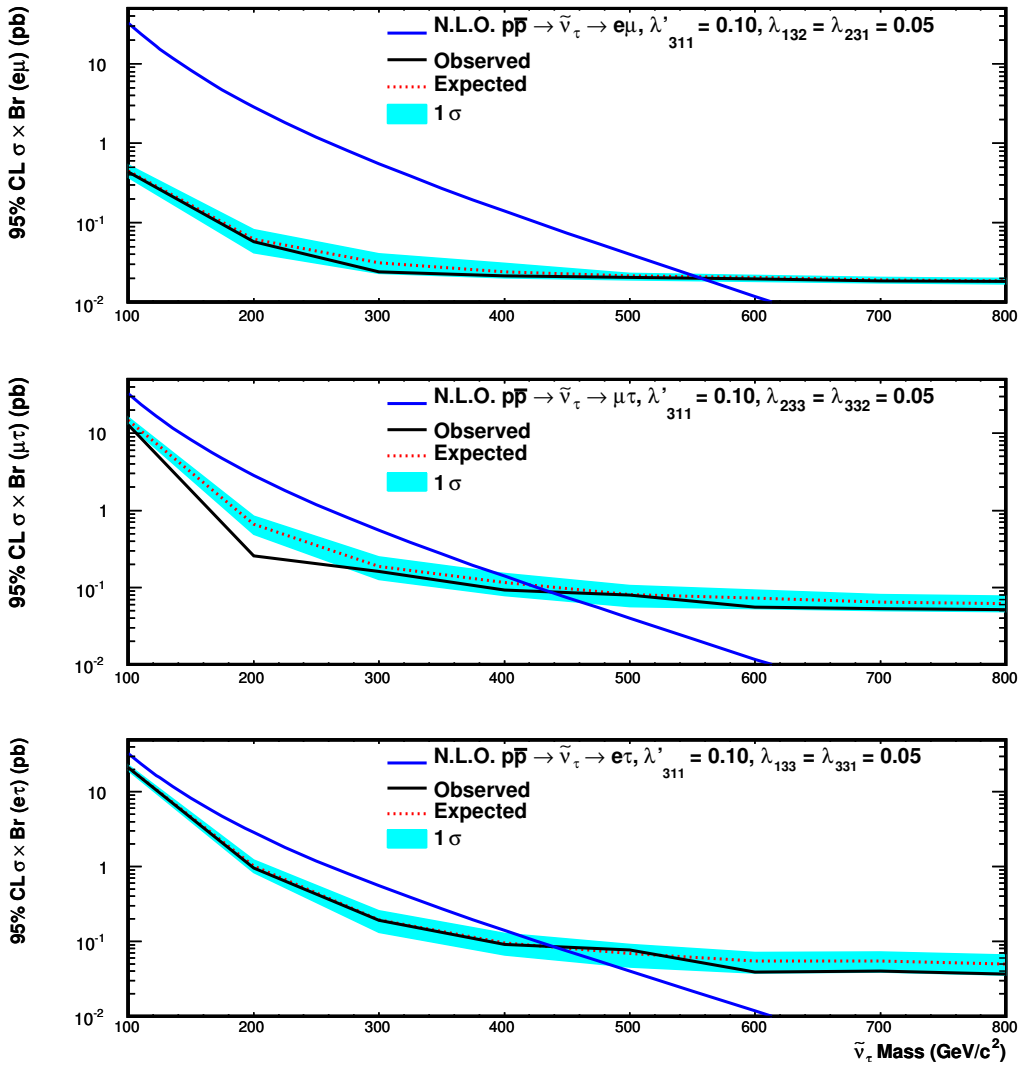

Figure 6.2: **95 % CL upper limits on the** $\sigma \times$ BR**.** The plots shows the expected and observed 95 % C.L. upper limits on the $\sigma \times$ BR $\widetilde{\nu}_\tau$ as a function of $\widetilde{\nu}_\tau$ mass. The theory cross sections are calculated at the benchmark point.

SM processes	eμ channel
	$M_{LL}^{min} = 500$ GeV/c^2
$Z/\gamma^* \rightarrow \tau\tau$	0.05 $\pm$ 0.1
$Z/\gamma^* \rightarrow \mu\mu$	0.0004 $\pm$ 0.0002
$W \rightarrow \mu\nu$(+jets)	< 0.0001
WW	0.01$\pm$ 0.001
$t\bar{t}$	0.001$\pm$0.001
Dijets and γ +jets	0.001$\pm$0.001
Total SM background	0.1$\pm$0.1$\pm$0.01
Observed Events in data	0

Table 6.3: **The Predicted Backgrounds and Observation in the Signal Region $M_{LL}^{min} = 500$ GeV/c^2 in $\mu\tau$ channel.** The uncertainties on the individual backgrounds are statistical and on the total predicted background are statistical and systematic.

$e\tau$ channel					
signal mass (GeV/c^2)	M_{LL}^{min} (GeV/c^2)	SM background events	observed events	exp. limit (pb)	obs. limit (pb)
100	> 80	332.4 ± 13.1	343	21.09	21.16
200	> 160	22.7 ± 1.4	21	1.02	0.96
300	> 230	5.0 ± 0.5	5	0.19	0.19
400	> 280	2.1 ± 0.4	2	0.096	0.092
500	> 310	1.4 ± 0.3	2	0.069	0.077
600	> 340	1.0 ± 0.3	0	0.055	0.039
700	> 360	0.9 ± 0.2	0	0.055	0.040
800	> 360	0.9 ± 0.2	0	0.050	0.037
$\mu\tau$ channel					
signal mass (GeV/c^2)	M_{LL}^{min} (GeV/c^2)	SM background events	observed events	exp. limit (pb)	obs. limit (pb)
100	> 80	153.1 ± 10.8	135	14.76	13.01
200	> 160	9.3 ± 1.3	2	0.66	0.26
300	> 220	2.6 ± 0.5	2	0.19	0.16
400	> 240	1.8 ± 0.4	1	0.12	0.093
500	> 280	1.0 ± 0.3	1	0.081	0.080
600	> 320	0.6 ± 0.2	0	0.072	0.056
700	> 350	0.4 ± 0.2	0	0.065	0.053
800	> 370	0.4 ± 0.2	0	0.062	0.052
$e\mu$ channel					
signal mass (GeV/c^2)	M_{LL}^{min} (GeV/c^2)	SM background events	observed events	exp. limit (pb)	obs.limit (pb)
100	> 90	22.8 ± 2.4	22	0.45	0.43
200	> 190	3.2 ± 0.5	3	0.062	0.058
300	> 280	0.6 ± 0.2	0	0.032	0.024
400	> 360	0.2 ± 0.2	0	0.024	0.022
500	> 450	0.1 ± 0.1	0	0.021	0.020
600	> 500	0.06 ± 0.1	0	0.021	0.020
700	> 550	0.05 ± 0.09	0	0.020	0.020
800	> 600	0.04 ± 0.08	0	0.019	0.018

Table 6.4: **Observations in Signal Regions.** Table shows that the number of observed events and the expectations from the SM background in eight signal regions in each channel. The observed 95% C.L. upper limits on $\sigma \times$ BR are also listed.

Chapter 7

Conclusion

We performed a search for high mass resonances decaying into two leptons of different flavor: $e\mu$, $e\tau$ and $\mu\tau$. The search is based on 1 fb^{-1} of CDF Run II data. We found good agreement between the SM predictions and observations. We set 95% C.L upper limits on the $\sigma \times$ BR of $\widetilde{\nu}_\tau \rightarrow e\mu/e\tau/\mu\tau$. Compared with the previous searches performed at CDF and D0, we improved the upper limit on the $\sigma \times$ BR of $\widetilde{\nu}_\tau \rightarrow e\mu$ and two new channels with the hadronic taus in final states are included. For the first time the RPV couplings related to the third generation leptons are constrained from a direct search. In the future, we can interpret the results in additional LFV scenarios, e.g. Z' and Higgs LFV decaying into the same final states. We can improve the analysis sensitivity with a larger dataset. In addition, we can further improve the sensitivity in the $e\tau$ and $\mu\tau$ channels, which currently have the lower signal acceptances compared to the $e\mu$ channel. Since the neutrino from tau decay escapes the detection and therefore contributes as missing transverse energy (MET), the dilepton mass, reconstructed from tau visible four-momentum, is lower that the real signal mass. However, our signal region definition is related to the reconstructed dilepton mass. For example, for $\widetilde{\nu}_\tau$ with mass 500 GeV/c^2, the signal region is defined as $M_{LL}^{min} = 310$ GeV/c^2 in the $e\tau$ channel and $M_{LL}^{min} = 280$ GeV/c^2 in the $\mu\tau$ channel. By adding the MET due to the neutrino into the reconstructed tau energy, we could

obtain a more narrow dilepton mass distribution, which allows us to increase the lower bound M_{LL}^{min} for the signal region. That will help us reduce the number of background events while not reducing the signal acceptance in the signal region.

Besides, the world's future highest energy accelerator, the Large Hadron Collider (LHC), with a center of mass energy of 14 TeV and a designed luminosity of 10^{34} cm^{-2}s^{-1}, will provide a chance for extraordinary discoveries on new physics. Many new particles are expected to be produced with a much larger cross section than that at the Tevatron. For instance, in the RPV MSSM scenario, the $\widetilde{\nu}_\tau$ production cross section at the LHC is larger than that at the Tevatron by about one order of magnitude at $M_{\widetilde{\nu}_\tau} \leq 200$ GeV/c^2, and about two orders of magnitude at $M_{\widetilde{\nu}_\tau} \geq 700$ GeV/c^2 when LHC reaches the designed feature [26]. This will significantly increases the potential for discovering the new particles in the first several years of operation. On the other hand, we must handle the more complicated collision environment, which needs a good understanding on the detector performance and the SM backgrounds. We will also have larger production rates of the SM backgrounds at the LHC. For instance, the rate for W boson production at the LHC is $\sim 10^5$ pb, Z production occurs at the $\sim 10^4$ pb, and the $t\bar{t}$ cross section is $\sim 10^3$ pb [25]. Nevertheless, given that the SM backgrounds are dominant in the relatively low mass region, the high-mass resonance searches are very promising at the LHC.

Appendix A

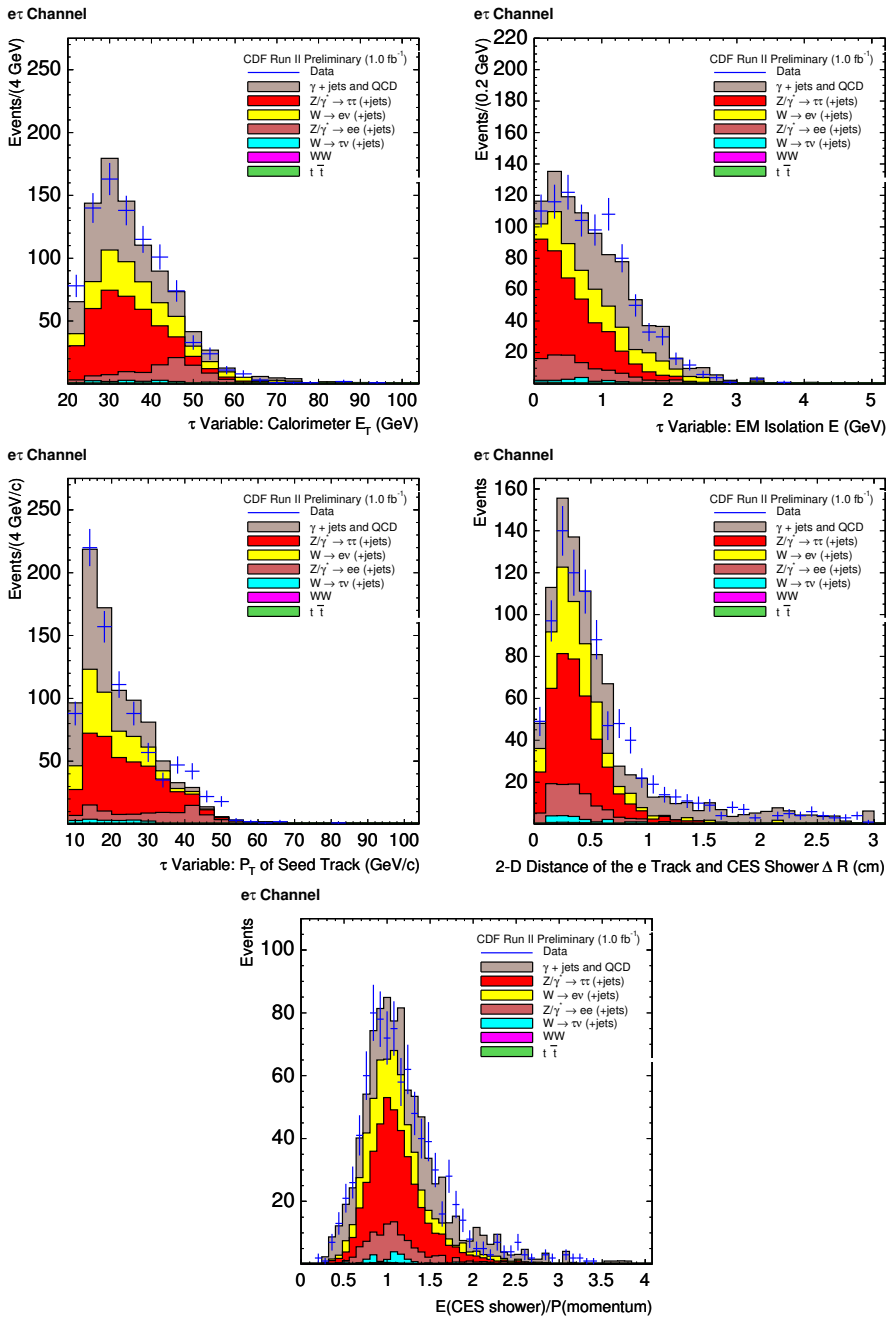

Figure A.1: **Distributions in the eτ channel control region.**

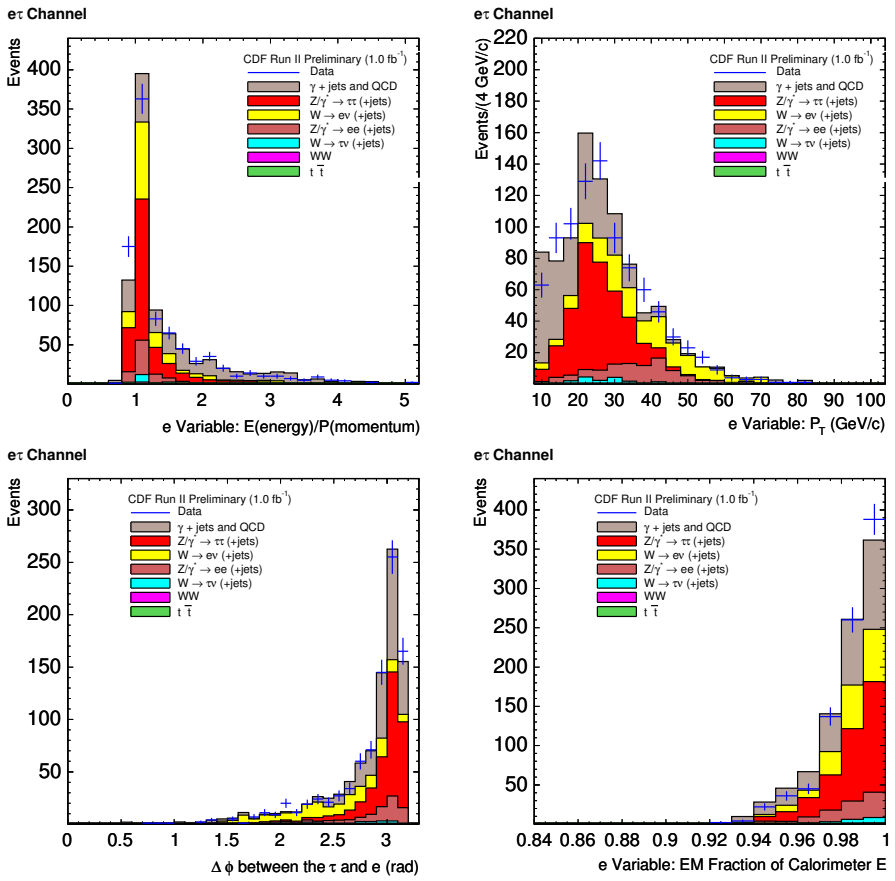

Figure A.2: **Distributions in the eτ channel control region.**

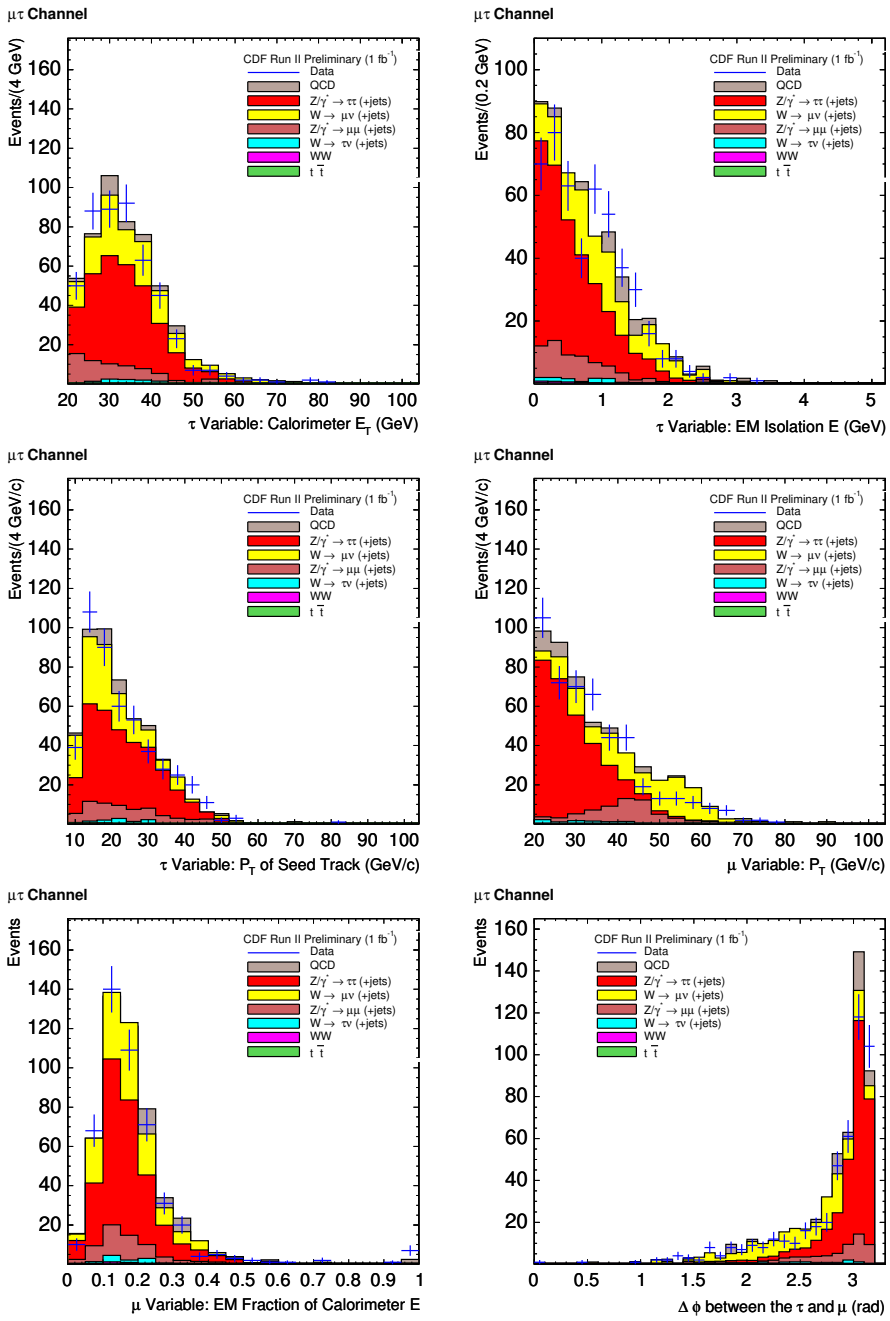

Figure A.3: **Distributions in the $\mu\tau$ channel control region.**

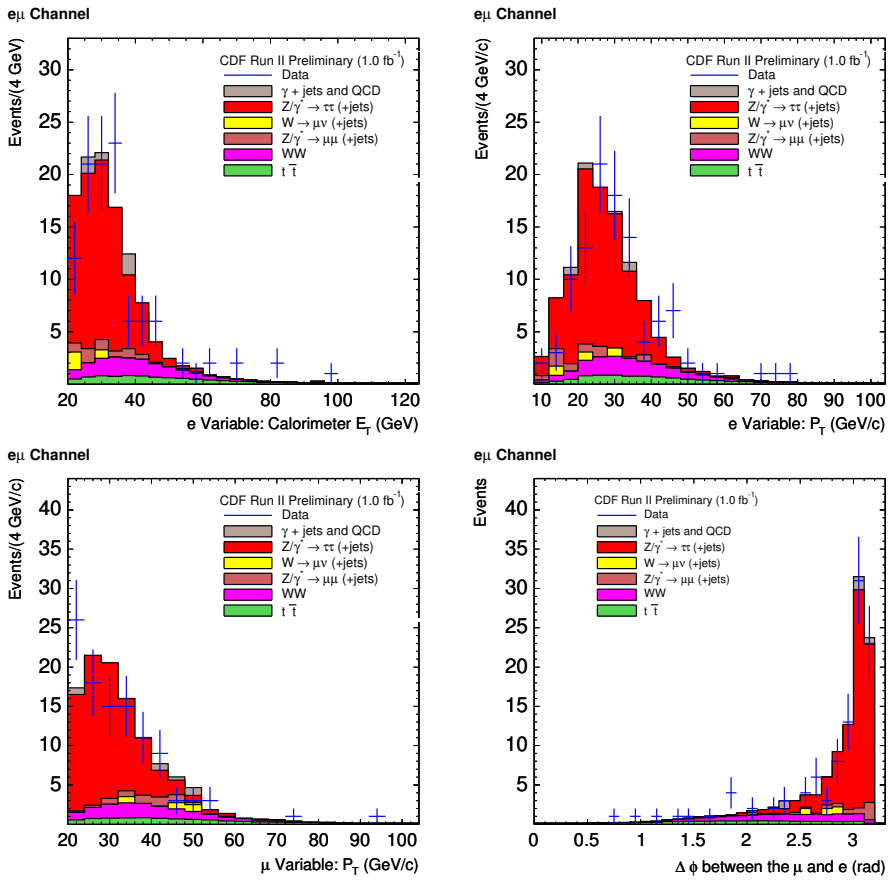

Figure A.4: **Distributions in the eμ channel control region.**

Bibliography

[1] F. Wilczek, arXiv:hep-ph/9802400.

[2] S. P. Martin, arXiv:hep-ph/9709356.

[3] M. Chemtob, Prog. Part. Nucl. Phys. **54**, 71 (2005) [arXiv:hep-ph/0406029].

[4] F. Ledroit and G. Sajot , GDR-S-008

[5] V. M. Abazov *et al.* [D0 Collaboration], Phys. Rev. Lett. **100**, 241803 (2008) [arXiv:0711.3207 [hep-ex]].

[6] A. Abulencia *et al.* [CDF Collaboration], Phys. Rev. Lett. **96**, 211802 (2006) [arXiv:hep-ex/0603006].

[7] P. Langacker and M. Plumacher, Phys. Rev. D **62**, 013006 (2000) [arXiv:hep-ph/0001204].

[8] B. Murakami, Phys. Rev. D **65**, 055003 (2002) [arXiv:hep-ph/0110095].

[9] T. Han and D. Marfatia, Phys. Rev. Lett. **86**, 1442 (2001) [arXiv:hep-ph/0008141].

[10] T. Han, H. E. Logan, B. Mukhopadhyaya and R. Srikanth, Phys. Rev. D **72**, 053007 (2005) [arXiv:hep-ph/0505260].

[11] A. Attal and A. Canepa, "Photon conversion removal efficiency", CDF internal note 8073.

[12] A. Anastassov etc, CDF public note 9071.

[13] P. Murat, Y. Tu, "Identification of the Hadronic Decays of Tau Leptons", CDF internal note 8470.

[14] P. Murat, Y. Tu, "Monte Carlo Modelling of the Jet to τ_h Fake Rates", CDF internal note 8809.

[15] C. DeBenedetti, Y. Tu, P. Murat, "Improved Method of Electron-Tau Separation", CDF internal note 9002.

[16] V. Martin, "High-P_T Muon ID Cuts and Efficiency for Use with 5.3.1 Data and 5.3.3 MC", CDF internal note 7367.

[17] Y. Ishizawa, J. Nielsen, "Trigger Efficiencies for High E_T Electrons", CDF internal note 7367.

[18] J. Nachtman and M. Schmitt, "Measurement of the Drell-Yan Cross Section", CDF internal note 8197.

[19] A. Sfyrla *et al.*, FERMILAB-CONF-07-548-E

[20] E. Thomson *et al.*, CDF public note 9448.

[21] J. Heinrich *et al.*, CDF public note 7117.

[22] D. E. Acosta *et al.* [CDF II Collaboration], Phys. Rev. Lett. **94**, 091803 (2005) [arXiv:hep-ex/0406078].

[23] S. Klimenko, J. Konigsberg, and T.M. Liss, FERMILAB-FN-0741 (2003).

[24] S.-M. Wang et al., Phys. Rev. D 74, 057902 (2006); Chinese Phys. Lett. Vol.25, No.1(2008)58.

[25] H. Baer, V. Barger and G. Shaughnessy, arXiv:0806.3745 [hep-ph].

[26] Y. Q. Chen, T. Han and Z. G. Si, JHEP **0705**, 068 (2007) [arXiv:hep-ph/0612076].